



**HAL**  
open science

## Thallium elemental and isotopic systematics in ocean island lavas

E.K.A. K A Brett, J. Prytulak, M. Rehkämper, S.J. J Hammond, C. Chauvel, A. Stracke, M. Willbold

► **To cite this version:**

E.K.A. K A Brett, J. Prytulak, M. Rehkämper, S.J. J Hammond, C. Chauvel, et al.. Thallium elemental and isotopic systematics in ocean island lavas. *Geochimica et Cosmochimica Acta*, 2021, 301, pp.187-210. 10.1016/j.gca.2021.02.035 . hal-03327717

**HAL Id: hal-03327717**

**<https://hal.science/hal-03327717v1>**

Submitted on 27 Aug 2021

**HAL** is a multi-disciplinary open access archive for the deposit and dissemination of scientific research documents, whether they are published or not. The documents may come from teaching and research institutions in France or abroad, or from public or private research centers.

L'archive ouverte pluridisciplinaire **HAL**, est destinée au dépôt et à la diffusion de documents scientifiques de niveau recherche, publiés ou non, émanant des établissements d'enseignement et de recherche français ou étrangers, des laboratoires publics ou privés.

## Thallium elemental and isotopic systematics in ocean island lavas

1  
2 <sup>1</sup>\*Brett, E. K. A., <sup>1,2</sup>Prytulak, J., <sup>1</sup>Rehkämper, M., <sup>3</sup>Hammond, S. J., <sup>4,5</sup>Chauvel, C.,  
3 <sup>6</sup>Stracke, A., <sup>7</sup>Willbold, M.

4  
5 <sup>1</sup>Department of Earth Science and Engineering, Imperial College London, London, UK, SW7 2BP

6 <sup>2</sup>Department of Earth Science, University of Durham, Durham, UK, DH1 3LE

7 <sup>3</sup>School of Environment, Earth and Ecosystem Sciences, The Open University, Milton Keynes, UK

8 <sup>4</sup>Université de Paris, Institut de Physique du Globe de Paris, CNRS, F-75005 Paris, France

9 <sup>5</sup>ISTerre, Université Grenoble Alpes, CNRS, Grenoble, France

10 <sup>6</sup>Institut für Mineralogie, Westfälische Wilhelms-Universität Münster, Corrensstraße 24, 48149 Münster,  
11 Germany

12 <sup>7</sup>Abteilung Isotopengeologie, Universität Göttingen, Goldschmidtstraße 1, 37077 Göttingen, Germany

13 \*corresponding author; email: a.brett13@imperial.ac.uk

14

15 Abstract word count: 340

16 Main text word count: 7843

17 Figures: 9

18 Tables: 6

19 Supplementary Materials: Appendix (683 words), 6 figures, 1 data annex (3 tables)

20 **Keywords:** thallium, stable isotopes, mantle heterogeneity, ocean island basalts

## 21 **Abstract**

22 The Earth's mantle exhibits marked chemical heterogeneity, sampled via oceanic basalts. We provide a  
23 comprehensive examination of thallium systematics in ocean island basalts (OIB): new high-precision trace  
24 element analyses, including Tl, and Tl isotopic compositions for 48 OIB spanning the entire range of  
25 observed Sr-Nd-Hf-Pb isotope ratios. All investigated OIB are characterised by ubiquitous Tl depletion  
26 requiring OIB mantle sources to have Tl concentrations as low as 0.2 ng/g, which is an order of magnitude  
27 lower than estimates for the primitive mantle and similar to Tl concentrations inferred for the depleted  
28 mantle. The low Tl concentrations inferred for OIB mantle sources are interpreted to reflect near quantitative  
29 removal of Tl during subduction and inefficient Tl recycling into the deeper mantle. If true, the Tl isotopic  
30 composition of surface materials may not be readily translated to the mantle sources of OIB.

31 The new OIB dataset shows a >10  $\epsilon$ -unit range in primary isotopic variation, from  $\epsilon^{205}\text{Tl} = -6.4$  to  $+6.6$ .  
32 However, the majority of samples (32 of 48) are within uncertainty of mantle values ( $\epsilon^{205}\text{Tl} = -2 \pm 1$ ), and  
33 show no co-variation with radiogenic isotopic composition. Notably, OIB with only minor Tl depletion (11  
34 samples) have Tl isotopic compositions outside the mantle range. The Tl concentration contrast between the  
35 mantle and inputs such as sediments and altered basalt is so great that minor additions (<1% by mass) of  
36 high-Tl material will dominate the isotopic budget of a lava, with decoupling of Tl and radiogenic isotopic  
37 compositions as an expected result. Thallium isotopic compositions of OIB are therefore difficult to link  
38 directly to radiogenic isotope variations and the mantle components they may reflect. Indeed, if isotopically  
39 distinct Tl from altered oceanic crust and/or sediments were efficiently recycled into the mantle and sampled  
40 via OIB, *more* variation in the Tl isotopic composition of OIB would be expected than is observed. The  
41 markedly unsystematic primary Tl isotopic variations in OIB therefore likely reflect the residual Tl isotopic  
42 composition of subducted material, and/or Tl acquired *en route* to the surface via shallow-level crustal  
43 assimilation.

## 44 **1. Introduction**

45 The majority of intraplate oceanic volcanism is the surface expression of deep-rooted thermochemical  
46 upwellings, or 'mantle plumes' (e.g. Morgan, 1971; Hofmann and White, 1982; Montelli et al., 2006). Ocean  
47 island basalts (OIB) thus provide a window into geochemical heterogeneity of the otherwise inaccessible  
48 deep mantle (e.g. White, 2015). Zindler and Hart (1986) first proposed a classification scheme for oceanic

49 basalts based on the observation that their radiogenic Sr-Nd-Pb isotope ratios vary systematically between a  
50 restricted number of isotopic signatures, termed ‘end-members’ or ‘components’. Decades of subsequent  
51 work has subdivided or refined the details and interpretations of the radiogenic Sr-Nd-Pb isotopic variability  
52 in oceanic basalts (e.g. Weaver, 1991; Chauvel et al., 1992; Hofmann, 1997; Workman and Hart, 2005;  
53 Willbold and Stracke, 2006). In general, the chemical variations observed in OIB can be reproduced via  
54 mixing of ambient mantle with other components, commonly identified with various recycled crustal  
55 lithologies (e.g. Hofmann and White, 1982; Weaver, 1991; Chauvel et al., 1992). Within this framework, it is  
56 suggested that the so-called HIMU (high  $\mu = {}^{238}\text{U}/{}^{204}\text{Pb}$ ) signature may represent ancient subducted oceanic  
57 crust, isolated for ~2 Ga, while enriched mantle (EM)-type signatures might represent incorporation of  
58 heterogeneous continental components in the form of clastic sediments or continental crust eroded at  
59 destructive plate margins (e.g. Hofmann and White, 1982; Zindler and Hart, 1986; Chauvel et al., 1992;  
60 Hofmann, 1997; Stracke et al., 2003, 2005; Willbold and Stracke 2006, 2010; Stracke, 2012).

61 Inferring mantle source compositions from the radiogenic isotope ratios observed in basalts is challenging,  
62 because sampling of the different source components via partial melting depends on a number of factors,  
63 such as initial concentrations, melting behaviour, partition coefficients, extent of melt mixing, and time  
64 elapsed between parent-daughter fractionation events. As a consequence, it is often difficult to reach  
65 unambiguous interpretations of the origins and history of mantle sources.

66 Resolving such ambiguities about the nature and origin of mantle composition and evolution on the basis of  
67 radiogenic isotopic variation observed in OIB is necessary to constrain global geochemical cycles and the  
68 Earth’s thermal evolution. Stable isotope systematics may provide useful independent constraints, as low-  
69 temperature surface environments have the potential to generate resolvable stable isotope fractionations,  
70 which might then be traced through subduction recycling into the mantle and subsequently sampled via OIB.  
71 Analytical advances have enabled the development and application of a variety of stable isotope systems to  
72 igneous rocks, motivated in part by the potential for such systems to act as a tracer of recycled materials.  
73 Many of these advances were recently reviewed in Teng et al. (eds), (2017), for stable isotope systems from  
74 Li to U. In general, larger isotope fractionations occur in surface environments than magmatic environments,  
75 and so a logical aim is to identify the incorporation of recycled surface material by determining whether  
76 magmatic rocks carry a stable isotopic signature that is distinguishable from the mantle.

## 77 **1.2 Thallium: a potential tracer for recycled materials**

78 Thallium is a highly incompatible element, conventionally grouped with the alkali elements due to the  
79 similar ionic radii of Tl<sup>+</sup> and the heavier alkali metals (e.g. Shaw, 1952; Heinrichs et al., 1980). The relative  
80 abundance of the two stable isotopes, <sup>205</sup>Tl (~70%) and <sup>203</sup>Tl (~30%), is reported as ε<sup>205</sup>Tl relative to the  
81 NIST SRM 997 Tl isotope standard (Rehkämper and Halliday, 1999):

$$82 \quad \epsilon^{205}\text{Tl}_{\text{SRM997}} = 10000 \cdot \left[ \left( \frac{{}^{205}\text{Tl}}{{}^{203}\text{Tl}}_{\text{sample}} - \frac{{}^{205}\text{Tl}}{{}^{203}\text{Tl}}_{\text{SRM997}} \right) / \left( \frac{{}^{205}\text{Tl}}{{}^{203}\text{Tl}}_{\text{SRM997}} \right) \right]$$

83 Thallium does not appear to undergo isotope fractionation during the high-temperature igneous processes of  
84 partial melting, metasomatism, and anhydrous fractional crystallisation. A systematic study of two co-genetic  
85 igneous suites spanning a range of SiO<sub>2</sub> contents from Iceland and the Mariana island arc found a restricted  
86 range in ε<sup>205</sup>Tl (Hekla: ε<sup>205</sup>Tl from -2.2 to -0.7; Anatahan: ε<sup>205</sup>Tl from -2.9 to 0.0), and indicates that no  
87 analytically resolvable Tl isotope fractionation occurs during anhydrous magmatic differentiation (Prytulak  
88 et al., 2017). Fitzpayne et al. (2020) analysed phlogopite mineral separates from highly metasomatised  
89 mantle xenoliths, again finding a strikingly restricted range in isotopic composition (ε<sup>205</sup>Tl = -2.5 ± 1.3 2sd, n  
90 = 25). This implies that the Tl isotopic composition of magmatic products should correspond to that of their  
91 sources, allowing the use of Tl isotope ratios to disambiguate the history of even evolved igneous rocks.

92 Direct measurements of Tl isotope ratios in mantle peridotites are hindered by their low concentrations (e.g.  
93 primitive mantle <4 ng/g: McDonough and Sun, 1995; 4.1 ng/g: Palme and O'Neill, 2014). However, a  
94 harzburgite analysed by Nielsen et al. (2015) with ε<sup>205</sup>Tl = -2.0 ± 0.8 (2sd), is indistinguishable from the Tl  
95 isotopic composition of MORB (ε<sup>205</sup>Tl = -2.0 ± 1.0 2sd; Nielsen et al., 2006a, 2017b), thus suggesting that Tl  
96 isotopes are not fractionated by partial melting processes.

97 Thallium elemental systematics in MORB are constrained by several large self-consistent (i.e. samples  
98 measured by the same protocols in the same laboratory) datasets collected in recent years, including well-  
99 calibrated high-precision Tl concentrations (Jenner and O'Neill, 2012; Nielsen et al., 2014; Yang et al.,  
100 2018).

101 Thallium concentrations are generally 100s to 10,000s of ng/g with large isotopic fractionations at the  
102 Earth's surface. The continental crust is the main terrestrial host of Tl (~500 ng/g e.g. Rudnick and Gao,  
103 2003; Jenner, 2017), with a Tl isotopic composition, inferred via loess, indistinguishable from MORB

104 (Nielsen et al. 2006b). Relative to the mantle, modern altered upper oceanic crust (AOC) has elevated Tl  
105 concentrations (~200 ng/g) and light Tl isotopic compositions ( $\epsilon^{205}\text{Tl} \sim -20$  to  $-5$ ; Nielsen et al., 2006b,  
106 2017b), whereas FeMn sediments have very high Tl contents (>10,000 ng/g) and preferentially incorporate  
107 the heavier Tl isotope ( $\epsilon^{205}\text{Tl} \sim +5$  to  $+15$ ; review of Nielsen et al., 2017b). The Tl concentration contrast  
108 spanning order of magnitude between the mantle and potential recycled components, coupled with the  
109 resolvable and opposite directions of isotope fractionation in surface materials relative to the mantle,  
110 theoretically makes Tl isotopic compositions extremely sensitive to contributions of recycled surface  
111 materials to the mantle. Indeed, previous work investigating subduction settings has shown that Tl isotope  
112 ratios of arc lavas can be directly linked to the isotopic composition of materials subducting outboard of the  
113 associated trenches (Prytulak et al., 2013; Nielsen et al., 2015, 2016, 2017a; Shu et al., 2017, 2019). By the  
114 same reasoning, Tl isotopic compositions may covary with traditional radiogenic isotope ratios in ocean  
115 island basalts, used to define mantle components. If some EM-type signatures reflect incorporation of  
116 recycled sediments, then isotopically heavy Tl is predicted. Likewise, if the HIMU OIB signature develops  
117 via input of AOC then HIMU lavas would be expected to exhibit isotopically light Tl.

### 118 **1.3 Sample selection and aims**

119 Previous Tl isotope studies of OIB have used the interpretive framework of isotopically heavy thallium  
120 indicating FeMn sediments and/or pelagic clays, and isotopically light thallium indicating AOC. Previous  
121 work has examined Hawai'i (Nielsen et al., 2006a), the Azores (Nielsen et al., 2007), Iceland (Nielsen et al.,  
122 2007; Prytulak et al., 2017), and St. Helena (Blusztajn et al., 2018), documenting a range of  $\epsilon^{205}\text{Tl} = -10$  to  
123  $+3.9$ . This large range is mostly due to variations in rocks from Hawai'i, ascribed to the addition of FeMn  
124 sediments, and St Helena, ascribed to the addition of AOC. Thus far, no published studies have examined  
125 EM-type lavas, or HIMU lavas from localities other than St Helena. Here, we investigate EM-type lavas and  
126 expand the number of HIMU localities, to better characterize the full range of known OIB sources. All  
127 selected samples have radiogenic isotope data and show limited evidence of alteration (e.g. low loss on  
128 ignition, freshness on inspection of thin section). The 48 new analyses comprise 32 EM-type (13 'EMI', 19  
129 other EM) and 16 HIMU lavas (Table 1). We aim to evaluate, on a global scale, the potential relationships  
130 between Tl elemental abundances, Tl stable isotopes, and radiogenic isotopic compositions in OIB to  
131 investigate the nature of mantle components and the efficiency of Tl cycling between crust and mantle.

## 132 **2. Methods**

133 Sample digestions and chemical separations were carried out in the MAGIC Laboratories, Imperial College  
134 London, as described in Brett et al. (2018). Purified water (resistivity 18.2 M $\Omega$  cm from a Milli-Q system)  
135 and acids purified via sub-boiling distillation in quartz or PTFE stills were used throughout.

### 136 **2.1 Trace element determination**

137 While Tl concentrations can be determined during isotope ratio measurements, early studies report  
138 uncertainties of 25% (e.g. Rehkämper et al., 2002), improved to ~10% by later work (e.g. Prytulak et al.  
139 2013) for relatively high concentration samples >20 ng/g. In contrast, the precision of Tl measurements via  
140 ICP-QQQ ('triple-quad' inductively coupled plasma mass spectrometer) is generally <4% RSD, though the  
141 uncertainty is higher for samples with lower Tl concentrations. Concentrations for 39 trace elements,  
142 including Tl, were obtained at the Open University, UK, using an Agilent 8800 ICP-QQQ following the  
143 procedure detailed in Brett et al. (2018).

144 In brief, for most samples approximately 50 mg of powder was weighed into a screw-top Savillex<sup>®</sup> PFA vial.  
145 To ensure precise and accurate determination of low Tl concentrations, ~75-100 mg of powder was weighed  
146 out for samples G6, FH-01, TH39, HV64, 74-386, and 108B. A 3:1 mixture of concentrated HF and HNO<sub>3</sub>  
147 was added to the vials, which were then heated to 140 °C for at least 24 hours. Samples were subsequently  
148 evaporated to *near* dryness, and dried down from 0.5-1 ml concentrated HNO<sub>3</sub> at 180 °C at least three times  
149 in order to destroy insoluble fluorides formed during the initial digestion. Samples were next taken up in 2  
150 ml 6M HCl, and refluxed at 120 °C for at least 24 hours, during which time they were ultrasonicated twice  
151 for 20 minutes, before being evaporated to complete dryness at 120 °C. 2 ml concentrated HNO<sub>3</sub> and 1 ml  
152 water were then added to each sample, followed by refluxing at 140 °C for at least 24 hours. Samples were  
153 again evaporated to dryness at 140 °C, before finally being made up to 1000-fold dilution in 2% HNO<sub>3</sub>.  
154 Sample solutions were aspirated using a quartz microflow nebuliser with an uptake rate of 0.5 ml min<sup>-1</sup>, with  
155 sensitivity on the order of 1-5 x 10<sup>7</sup> cps per  $\mu$ g/ml, depending on the element. Two collision/reaction gas  
156 configurations were used: no gas, for Tl and most other elements, and O<sub>2</sub>, for most Rare Earth Elements (see  
157 Brett et al., 2018). In the no gas configuration, oxide levels, measured as CeO<sup>+</sup>/Ce<sup>+</sup>, were kept below 1%;  
158 double-charged species, measured as Ce<sup>2+</sup>/Ce<sup>+</sup>, were kept at 1.6%.

159 All elements except Tl were calibrated using the values provided in Eggins et al. (1997) for USGS reference  
160 materials (RMs) W-2 and DNC-1. For Tl, USGS RMs BIR-1, BHVO-2 and AGV-1 were used as calibrators,  
161 employing the values of Brett et al. (2018). Calibrator materials were run at the beginning of each  
162 measurement session. An internal solution standard (with Be, Rh, In, Tm, Re, Bi) was added online to  
163 monitor and correct instrumental drift. Drift was further monitored after every five measurements of  
164 unknown solutions with a measurement block comprising GSJ RM JB-2, 2% HNO<sub>3</sub>, and a repeated unknown  
165 sample (G-6).

## 166 **2.2 Thallium isotope ratio determination**

167 Procedures for Tl separation and subsequent measurement of Tl isotopic compositions followed established  
168 protocols. Briefly, all procedures were carried out at the MAGIC Laboratories, Imperial College London.  
169 Samples were digested via standard HF-HNO<sub>3</sub> techniques, and Tl isolated from the matrix using a 2-stage  
170 ion exchange chromatography procedure detailed in Rehkämper and Halliday (1999) and Nielsen et al.  
171 (2004), with modifications as described in Brett et al. (2018). The majority of isotope ratio measurements  
172 were performed using a *Nu HR MC-ICP-MS* equipped with 10<sup>11</sup> Ω resistors, as low resolution measurements  
173 using a ~100 µl/min flow rate nebuliser connected to an *Aridus*, *Aridus II* or *Nu DSN* desolvating system,  
174 with Tl solutions ranging in concentration from 2-5 ng ml<sup>-1</sup> and a sensitivity of ~800 V/ppm Tl.

175 The limited availability of powder for some OIB samples, coupled with low Tl concentrations, required  
176 measurement of solutions with Tl concentrations of <1 ng/ml. Measurements of these low-concentration  
177 analytes on the *Nu HR MC-ICP-MS* are less precise than those of solutions with 2-5 ng/ml Tl. Measurements  
178 on a *Nu Plasma II MC-ICP-MS* during the later phase of the project have significantly increased sensitivity  
179 compared to the *Nu HR MC-ICP-MS*. For Tl, sensitivity on the *Nu Plasma II* was routinely well in excess of  
180 1000 V/ppm at the same measurement conditions. Otherwise, the method for isotope ratio determination on  
181 the *Nu Plasma II* was identical to the *Nu HR*, as described in Brett et al. (2018).

182 A secondary Tl isotope reference solution from Aldrich ('Aldrich Tl solution'), first characterised by  
183 Rehkämper and Halliday (1999), is routinely used (>2000 measurements across at least seven laboratories;  
184 Nielsen et al., 2017b) to monitor machine performance. At least two measurements of the Aldrich Tl solution  
185 were performed at the beginning and end of each session, with additional measurements performed

186 throughout, typically after every 6 unknown samples. Additionally, a well-characterised USGS reference  
187 material (typically BCR-2, though AGV-2 and BHVO-2 were also used) was processed through the complete  
188 sample preparation procedure with every batch of 10 samples prepared for MC-ICP-MS analysis.

189 **Powder leaching tests.** Thallium can be concentrated in secondary clays and ferromanganese coatings. To  
190 assess possible effects of secondary, low-temperature alteration processes on Tl isotopic composition,  
191 powder leaching experiments were performed. Samples with isotopic compositions that differed from  
192 average MORB by more than 3  $\epsilon$  units, as determined on unleached powders, were chosen for these leaching  
193 experiments.

194 The leaching protocol followed the cold acid leaching of Weis and Frey (1991). Approximately 10 ml 6M  
195 HCl was added to 100-300 mg of a sample powder, and the suspension was ultrasonicated for 30 minutes.  
196 After settling for at least 30 minutes, the leachate was drawn off and discarded, and a further ~10 ml 6M HCl  
197 was added to samples, which were then ultrasonicated again for 20-30 minutes. This process was repeated  
198 until the leachate ran clear (a minimum of 3 cycles), and was then repeated a further 2 times with purified  
199 water in place of HCl. Leached powders were then evaporated, digested, separated and measured in the same  
200 manner as unleached powders.

## 201 **3. Results**

### 202 **3.1 Trace element concentrations**

203 Table 2 lists key major and trace element concentrations for the 48 OIB samples. Thallium concentrations  
204 range from 7 to 235 ng/g. The full dataset of 39 elements is provided in Electronic Annex 1 along with  
205 results for the reference materials measured contemporaneously with the OIB samples. Trace element  
206 concentrations obtained for repeated measurement of BCR-2 and JB-2 are in good agreement with accepted  
207 values (Electronic Annex 2). For most elements, RSDs are generally <3%; for Tl, RSDs are <7% for 34  
208 samples, and >10% for 5 samples (Electronic Annex 2).

209 Many samples have existing trace element data published on the same powders (Electronic Annex 2, 3), and  
210 there is generally good agreement with previous work. We emphasize that the new data pays particular  
211 attention to the calibration of Tl concentration measurements, and is therefore be used throughout the  
212 remainder of this work.

### 213 3.2 Thallium isotope ratios

214 Table 2 presents the Tl isotopic composition of the 48 global OIB measured in this study, highlighting  
215 samples with isotopic compositions determined for both leached and unleached powders. Thallium isotopic  
216 compositions range from -6.4 to +6.6 and do not co-vary with Tl concentrations (Fig. 1). The quoted  
217 uncertainties take into account the measurement instrument and signal intensity, and are reported as the  
218 highest of (1) the uncertainty for repeat analyses of BCR-2 on the *Nu HR*, (2) the uncertainty for repeated  
219 measurements of the Aldrich Tl solution on the *Nu Plasma II*, or (3) the uncertainty for repeat analyses of a  
220 given sample.

221 The long-term intermediate precision of the Aldrich Tl solution measured on the *Nu HR* contemporaneously  
222 with OIB samples was  $\epsilon^{205}\text{Tl} = -0.8 \pm 0.4$  (2sd;  $n = 211$ , 14 sessions, 4 years), calculated using the average  
223  $\epsilon^{205}\text{Tl}$  values obtained during each measurement session due to the large number of analyses. Unleached  
224 digestions of USGS reference materials AGV-2 (1), BCR-2 (10) and BHVO-2 (2) yielded  $\epsilon^{205}\text{Tl}$  values of -  
225  $2.9 \pm 0.5$  (2sd;  $n = 3$ , 1 session),  $-2.6 \pm 0.5$  (2sd;  $n = 21$ , 4 sessions), and  $-1.2 \pm 0.8$  (2sd;  $n = 3$ , 1 session) for  
226 measurements with signal intensity on mass 205 > 1 V. For measurements of BCR-2 (4 digestions) with  
227 signal intensity < 1 V,  $\epsilon^{205}\text{Tl} = -2.5 \pm 1.3$  (2sd;  $n = 21$ , 3 sessions). For both Aldrich solution and USGS  
228 RMs, many of these determinations were first reported in Brett et al. (2018) and the values obtained are in  
229 good agreement with previous compilations (Nielsen et al., 2017b; Prytulak et al., 2017).

230 The average obtained for the Aldrich Tl solution on the *Nu Plasma II* was  $\epsilon^{205}\text{Tl} = -0.8 \pm 0.8$  (2sd;  $n = 28$ , 2  
231 sessions, 2 months), with the higher uncertainty reflecting both the smaller number of analyses and the lower  
232 concentration of solutions. One unleached dissolution of BCR-2 yielded  $\epsilon^{205}\text{Tl} = -3.1 \pm 0.8$  (2sd;  $n = 1$ ),  
233 while one leached dissolution yielded  $\epsilon^{205}\text{Tl} = -2.1 \pm 0.8$  (2sd,  $n = 1$ ), demonstrating that our leaching  
234 procedure does not introduce resolvable  $\epsilon^{205}\text{Tl}$  fractionations.

### 235 3.3 Assessing secondary effects on Tl isotope ratios

236 **Melt evolution.** Many stable isotope systems display isotope fractionation during fractional crystallisation  
237 (e.g. Teng et al., 2017). Thallium behaviour has been previously been investigated using two cogenetic suites  
238 with invariant radiogenic isotopic compositions from different tectonic settings: Hekla, Iceland, and  
239 Anatahan, Marianas (Prytulak et al., 2017). Neither suite fractionates hydrous phases, nor do they exhibit

240 resolvable Tl isotope fractionation during differentiation. Rader et al. (2018) show that hydrous K-rich  
241 phases such as micas can exhibit distinct Tl isotopic compositions ( $\epsilon^{205}\text{Tl}$  from -12.1 to +5.3) coupled with  
242 significant Tl enrichments ( $>5 \mu\text{g/g}$ ). As such, while it is not possible to completely rule out crystallisation-  
243 induced fractionation, it is highly unlikely for the OIB studied here. With the caveat that our samples are not  
244 genetically related, there is no systematic variation of  $\epsilon^{205}\text{Tl}$  with inferred or observed phenocryst phases or  
245 with MgO content in the current dataset (Fig. S1). We thus do not exclude any samples on this basis.

246 **Degassing.** Magmatic degassing can induce kinetic Tl isotope fractionation (Baker et al., 2009), theoretically  
247 producing residues with heavy Tl isotopic compositions and low Tl concentrations relative to incompatible  
248 refractory elements in contrast with condensates with isotopically light Tl, though these have yet to be  
249 reliably identified in nature. Various ratios have been employed to assess sample degassing, including Th/Tl  
250 (Nielsen et al., 2007), Pb/Tl (Rehkämper and Nielsen, 2004; Baker et al., 2009), Cs/Tl (Prytulak et al., 2013)  
251 and Ce/Tl (Nielsen et al., 2017a). The use of such ratios is challenging: Nielsen et al. (2017a) note that in arc  
252 settings, high Ce/Tl ratios potentially indicative of kinetic processes are still lower than the average value for  
253 the upper mantle. In the current dataset, there is no co-variation indicative of degassing between  $\epsilon^{205}\text{Tl}$  and  
254 relevant trace element concentrations or ratios for samples from individual volcanoes (not shown). This lack  
255 of chemical evidence is coupled with a lack of textural evidence for significant degassing, in that samples are  
256 thought to have been emplaced during effusive eruptions and show no significant vesicularity. Therefore, no  
257 data are rejected on this basis.

258 **Post-depositional effects.** In submarine lavas, both contamination (increasing the Tl contents of the rocks)  
259 and alteration (decreasing the Tl contents, via weathering) potentially cause resolvable differences in  $\epsilon^{205}\text{Tl}$ .  
260 As little as  $1 \mu\text{g}$  of FeMn oxyhydroxide coating per gram of sample can cause an analytically resolvable shift  
261 to heavier isotope signatures, while submarine alteration may efficiently strip Tl (at high temperatures) or  
262 add isotopically light Tl (at low temperatures) (Nielsen et al., 2006a). Samples exhibiting very low Tl  
263 concentration and  $\epsilon^{205}\text{Tl}$  therefore require scrutiny for other evidence of alteration, whereas samples with  
264 very high Tl concentration and extreme  $\epsilon^{205}\text{Tl}$  require scrutiny for contamination. A good example of the  
265 effects of alteration on Tl concentrations and isotopic compositions is provided by the study of Bluzstajn et  
266 al. (2018) on St. Helena lavas. In this case, a sample (SH-75) was excluded due to its high Tl concentration  
267 ( $339 \text{ ng/g}$ ) combined with an isotopic composition of  $\epsilon^{205}\text{Tl} = -4.06$  and visual evidence of alteration. The

268 authors consider surficial contamination by secondary clay minerals to be the most likely explanation for  
269 these features.

270 All OIB lavas analysed in this study were collected subaerially, although ambiguous records mean that it is  
271 unclear if the oldest Rurutu lavas were erupted in a subaerial or submarine environment (Chauvel et al.,  
272 1997). One Rurutu lava (RRT-037) shows the highest  $\epsilon^{205}\text{Tl}$  value ( $6.6 \pm 0.5$  2sd) reported for oceanic basalts  
273 thus far, warranting further assessment. However, rather than relying solely on chemical variation to identify  
274 such effects, five samples with  $\epsilon^{205}\text{Tl}$  signatures significantly different from the mantle value were leached  
275 and reanalysed alongside USGS reference material BCR-2. The residues from the cold HCl leach retained  
276 1% to 50% of the original Tl, resulting in 0.05 to 1.9 ng/g total Tl available for analysis ( $\sim 6$  ng/g for BCR-2),  
277 thus resulting in larger analytical errors for  $\epsilon^{205}\text{Tl}$  (typically about  $\pm 1$   $\epsilon$ ). Notably, there is no systematic  
278 offset in  $\epsilon^{205}\text{Tl}$  for the leached relative to the unleached sample powders (Table 2). This provides strong  
279 evidence that the positive and negative  $\epsilon^{205}\text{Tl}$  end-members in our dataset are not due to surficial  
280 contamination. Therefore, we do not exclude any samples on this basis.

281 Assessment of subaerial post-depositional alteration is more challenging. These processes may remove Tl  
282 from the sample without significant Tl isotope fractionation. While large fractionations do arise in low-  
283 temperature environments, strong mineralogical control is exerted by secondary sulphides in low-T  
284 hydrothermally altered oceanic crust (Coggon et al., 2014) and by birnessite in FeMn sediments (Peacock  
285 and Moon, 2012; Nielsen et al., 2013). Suspended riverine particulate matter, created through weathering,  
286 exhibits  $\epsilon^{205}\text{Tl}$  very similar to that of loess, with the oxyhydroxide fraction generally containing only minor  
287 Tl that is not isotopically distinct (Nielsen et al., 2005). However, loss on ignition (LOI) is a traditional  
288 qualitative indicator of such alteration. All 48 analysed samples have LOI < 4%, and 41 have LOI < 2%. The  
289 seven samples with LOI > 2% were described as showing no identifiable petrological evidence of alteration  
290 (see Table 1 and references therein). Therefore, no data are excluded on this basis.

## 291 **4. Discussion**

292 We combine our new dataset with published studies to explore Tl behaviour at constructive plate margins  
293 and in intraplate settings. We first revisit the relative compatibility of Tl during mantle melting, then present  
294 models of Tl behaviour during MORB and OIB melting. Finally, we examine Tl isotope systematics

295 alongside Sr-Nd-Pb radiogenic isotopic compositions in the global OIB dataset to explore implications for  
296 cycling of Tl through the solid Earth.

#### 297 **4.1 Tl elemental systematics**

298 Thallium is highly incompatible during magmatic processes. Absolute Tl concentrations in OIB are thus  
299 principally determined by the extent of partial melting and fractional crystallisation. To compare the  
300 geochemistry of samples representing different degrees of melting, normalised incompatible element  
301 diagrams and ratios of trace elements with similar chemical partitioning are often employed. Quantitative  
302 assessment of how similarly two elements partition is theoretically straightforward: in a log-log plot of  
303 element concentrations, pairs of elements that partition identically produce a linear trend with a slope of  
304 unity (e.g. Sims and DePaolo, 1997). Such assessments are improved by taking into account the uncertainties  
305 in concentration for *both* elements (e.g. by using York regressions: York et al., 2004; Reed, 2010). In reality,  
306 however, analytical and statistical errors potentially obscure small deviations from linearity, especially  
307 between highly incompatible elements. It is therefore important to keep in mind that such relationships are at  
308 best indicative of relative compatibility contrasts. For MORB data, Nielsen et al. (2014) calculated that La,  
309 Ce, and Pb had partitioning most similar to Tl, with  $\log[\text{Tl}] - \log[\text{Ce}]$  yielding a slope of  $0.999 \pm 0.034$  (2sd,  
310  $n = 594$ ). Results for the expanded dataset incorporating Yang et al. (2018) are very similar (Table 3).

311 OIB clearly derive from heterogeneous sources. As such there is no expectation that log-log plots would  
312 provide anything other than a very approximate indication of relative partitioning. Indeed, even for samples  
313 from a single location there is a marked lack of coherence in log-log diagrams of Tl versus any trace element  
314 (not shown). Of all analysed elements, the closest approach to a slope of unity with  $\log[\text{Tl}]$  is achieved for  
315  $\log[\text{Rb}]$ , as found by Dupuy et al. (1973) for acidic volcanic rocks (Table 3). However, the uncertainty is so  
316 high that this is not a robust result. While lower uncertainties are achieved for  $\log[\text{Ce}]$  and  $\log[\text{La}]$ , the slope  
317 does not approximate unity. Attempting to identify elements with similar bulk partition coefficients to Tl  
318 during OIB generation via log-log plots is therefore problematic.

319 **Normalised incompatible element diagrams.** Thallium has been placed both between La and Ce, for low-  
320 pressure fractionation of MORB (Jenner, 2017), and between Cs and Rb (Prytulak et al., 2017, following  
321 Dupuy et al., 1973). Given the ambiguity regarding placement and the lack of compelling indications from

322 log-log plots, we consider both compatibility orderings for the presentation of OIB data. Incompatible  
323 elements normalised to PM abundances are shown in Figure 2 (with normalisation to DM shown in Fig. S2).  
324 Notable is the marked negative Tl anomaly compared to other large-ion lithophile elements (47 of 48  
325 samples) and REE (all samples). The La-Tl-Ce ordering produces visually similar Tl depletions to elements  
326 that are fluid-mobile during subduction processing, particularly Pb. The co-variation is less striking for the  
327 Cs-Tl-Rb ordering, which might reflect the larger uncertainties of Cs abundances and/or the inferred greater  
328 similarity in fluid-mobile behaviour. Interestingly, the magnitude of the negative Tl anomaly co-varies with  
329 absolute Tl abundance, regardless of ordering (Fig. S3). Such co-variation would be anticipated if the  
330 ambient mantle contains negligible Tl, such that increasing Tl abundances from exotic source(s) correlate  
331 directly with less negative Tl anomalies. In this scenario, the normalising PM (and DM) Tl concentration  
332 would be overestimated.

333 **‘Invariant’ trace element ratios.** Ratios of trace elements with similar partitioning are commonly used to  
334 ‘see through’ the effects of magmatic evolution: where partitioning is identical, ratios should be identical in  
335 source and product. However, selecting a suitable ratio for Tl in OIB is challenging. The Cs/Tl ratio has been  
336 used, as partitioning of these two elements and their fluid mobility was assumed to be similar (e.g., Nielsen  
337 et al., 2006a; Prytulak et al., 2013; 2017). However, Cs/Tl can be affected by both degassing and possible  
338 sequestration of Tl in accessory minerals during subduction (e.g., Prytulak et al., 2013) and although Cs  
339 concentration determinations are routinely performed during ICP-MS analyses they often have relatively  
340 large errors due to the low abundance of Cs in igneous systems. The Ce/Tl ratio has also been used to assess  
341 Tl systematics in igneous settings, and has the advantage of a limited range in MORB (e.g. Nielsen et al.,  
342 2014, 2017b). As Tl partitioning is likely different between MORB and OIB regimes, no single ratio will be  
343 invariant for both tectonic settings.

344 In the new OIB dataset, Ce/Tl varies over an order of magnitude at a similar degree of magmatic  
345 differentiation. While absolute Tl concentrations in OIB vary with MgO content, taken as a measure of the  
346 extent of differentiation, Ce/Tl ratios do not (Fig. 3). Therefore, the range of Ce/Tl in OIB likely arises from  
347 some combination of source heterogeneity and melting processes. For example, Shu et al. (2019) observed a  
348 wide range of Ce/Tl in subducted eclogites, which are geochemically similar to altered subducted oceanic  
349 crust that is thought to be a common component in OIB sources. Some authors have noted generally higher

350 Ce/Tl ratios in OIB compared to MORB (Nielsen et al., 2014; Blusztajn et al., 2018). When examining all  
351 available data, a clear tectonic distinction between MORB, arc and OIB lavas is apparent (Fig. 4): (1) arc  
352 lavas generally exhibit the lowest Ce/Tl and highest Tl concentrations, alongside the most scattered  
353 distribution, even when filtered to exclude non-basaltic samples; (2) MORB Ce/Tl clusters around 1140, as  
354 previously discussed in Nielsen et al. (2014), and (3) global OIB form a remarkably coherent array that is  
355 clearly distinct from MORB, with overlap between the different mantle components defined by radiogenic  
356 isotopes. Similar patterns are observed for ratios of Tl with Rb, Cs, La and Pb, though with these latter ratios  
357 the different tectonic settings are less clearly distinguished (Fig. S4), motivating the further focus on Ce/Tl  
358 systematics.

#### 359 **4.2 Modelling Tl variations in MORB and OIB**

360 The systematic variation of Tl versus Ce/Tl in global MORB and OIB can be explored with simple melting  
361 and mixing models (Fig. 5, 6). Fractional, non-modal melting models help explore the contrasting Ce/Tl  
362 patterns of MORB and OIB, though simplifying assumptions must be made for several parameters (Tables 4-  
363 6). Nielsen et al. (2014) identified constraints for the majority of these parameters for MORB generation, and  
364 modelled production of the “near-uniform” Ce/Tl ratio for MORB through variation of S concentrations and  
365 associated  $D_{\text{sulf/sil}}^{\text{Tl}}$  values. However, subsequent findings warrant some re-evaluation of parameters.

366 While it is clear that Tl is hosted in sulphides to some extent, recent investigations into the partitioning of Tl  
367 indicates that it is less strongly chalcophile than previously assumed (e.g. Kiseeva and Wood, 2015; Wood  
368 and Kiseeva, 2015; Jenner, 2017; and see Appendix for detailed discussion). We therefore explored  $D_{\text{sulf/sil}}^{\text{Tl}}$   
369 values between 1 and 25 and present results for  $D_{\text{sulf/sil}}^{\text{Tl}} = 10$  (e.g. Kiseeva and Wood, 2013, 2015; see  
370 Appendix for detailed discussion). We also consider the effects of variation in  $D_{\text{cpx/melt}}^{\text{Ce}}$  between 0.01 and  
371 0.8, which encompasses the wide range attributed to differences in mineral chemistry (Table 5; Appendix).

372 **MORB.** The MORB dataset in Figure 5 combines the studies of Jenner and O’Neill (2012), Nielsen et al.  
373 (2014) and Yang et al. (2018), excluding samples with MgO < 6wt%, seamounts, back-arc basins and  
374 aseismic ridges. These studies yield a combined mean MORB Ce/Tl of  $1220 \pm 570$  (2sd, n = 909).

375 Fractional melting models assuming a spinel lherzolite source with variations in  $D_{\text{cpx/melt}}^{\text{Ce}}$  and initial  
376 elemental concentration are shown in Figure 5, with the fractional melting model of Nielsen et al. (2014)

377 reproduced in Figure 5a. We explore a range of  $D_{\text{cpx/melt}}^{\text{Ce}}$  in Figure 5b, reproducing not only the average  
378 Ce/Tl value observed for MORB but also the sense of variation in the data. Compared to the model of  
379 Nielsen et al. (2014), the reduced compatibility of Tl in sulphides means that the model is less sensitive to  
380 the S concentration of the upper mantle. Considering only variations in the bulk partitioning of Ce, over 80%  
381 of MORB samples can be explained with a range of  $D_{\text{cpx/melt}}^{\text{Ce}}$  up to  $\sim 0.35$ . Furthermore, about 50% of  
382 MORB samples are explained by  $D_{\text{cpx/melt}}^{\text{Ce}} \leq 0.2$ , while fewer than 2% of MORB samples require  $D_{\text{cpx/melt}}^{\text{Ce}}$   
383  $\geq 0.8$ .

384 We also present the effects of variation in initial Tl and Ce concentration on our melting model (Fig. 5c, 5d;  
385 Appendix), with  $D_{\text{cpx/melt}}^{\text{Ce}} = 0.1$  (equivalent to bulk  $D^{\text{Ce}} = 0.015$ , i.e. the average value for peridotite melting  
386 calculated by Stracke and Bourdon, 2009). Again, variation in either of these parameters can account for  
387 both the average Ce/Tl ratio in MORB and the sense of the observed variation.

388 The models thus highlight two main points.

- 389 1. As previously noted, MORB Ce/Tl exhibits some variation with Tl concentration that exceeds  
390 measurement uncertainties (Nielsen et al., 2014). We suggest that Ce/Tl variations in MORB can be  
391 explained through a combination of melting effects, a range of  $D_{\text{cpx/melt}}^{\text{Ce}}$  associated with variations in  
392 the mineral composition of clinopyroxene, and variations in source concentrations of Tl and Ce.  
393 Notably, this model does not require that bulk partition coefficients for Ce and Tl be approximately  
394 equal, and is nonetheless able to satisfy the constraint that a log-log concentration plot should exhibit  
395 a slope close to unity given the observed maximum concentration of Tl in MORB.
- 396 2. Regardless of the chosen value of  $D_{\text{cpx/melt}}^{\text{Ce}}$ , a model incorporating lower compatibility of Tl in  
397 sulphides than previously assumed yields a best fit for a  $\text{Tl}_{\text{DM}}$  abundance of 0.27 ng/g. This value is  
398 calculated assuming that (i) samples with the lowest Tl concentrations on average represent the  
399 highest degree of melting, i.e. the closest approach to the DM Ce/Tl ratio, and (ii) an average  $\text{Ce}_{\text{DM}}$   
400 of 0.55  $\mu\text{g/g}$  (Workman and Hart, 2005). Our proposed  $\text{Tl}_{\text{DM}}$  is considerably lower than the estimate  
401 of Salters and Stracke (2004) of 0.38 ng/g, and much lower than that of Nielsen et al. (2014) of 0.48  
402 ng/g.

403 **OIB.** Fractional melting models assuming either a PM or a DM source (Table 4) with up to 15% melting are  
404 shown in Fig. 6a. It is immediately apparent that partial melting alone cannot produce the observed OIB  
405 Ce/Tl array from a PM or DM source, even for extreme values of  $D^{\text{Ce}}_{\text{cpx/melt}}$ . The systematics in a plot of  
406 Tl/Ce versus Tl (Minster and Allègre, 1978; Fig. S5) emphasise that the observed range exceeds that which  
407 can be explained by partial melting and fractional crystallisation alone, consistent with longstanding  
408 radiogenic isotopic evidence for the heterogeneous and mixed nature of OIB sources. Notably, variations in  
409 S concentration or  $D^{\text{Tl}}_{\text{sulf/sil}}$  have no significant effect on model fit, but do affect the required degree of partial  
410 melting.

411 To explain the variation in the OIB array we first establish constraints on the mixed source compositions. In  
412 this context, solid state mixing is assumed, rather than mixing of partial melts of distinct components.  
413 Parameters including partition coefficients and initial elemental concentrations were varied until approximate  
414 matches between model output and the observed data array for up to 15% melting were achieved (Fig. 6b).  
415 We then incorporate the assumption that OIB lavas are typically the product of ~3-5% melting. In this  
416 scenario, the required source materials vary over an order of magnitude in terms of Tl concentration even  
417 within a single island (Fig. 6c, 6d). A striking feature of the model is that the majority of the array requires a  
418 source that is significantly more enriched in Ce than PM estimates, *without* similar enrichment in Tl. Indeed,  
419 most lavas require Tl source concentrations lower than PM estimates, and in some instances more depleted  
420 than DM. Of all the OIB samples analysed to date ( $n = 93$ ) only 10 (~11%) require a source Tl concentration  
421  $>3.5$  ng/g, i.e. more enriched in Tl than PM. Notably, although lavas from individual islands require source  
422 heterogeneity in terms of Tl concentration, lavas representing distinct radiogenic isotopic compositions have  
423 overlapping Ce/Tl ranges.

424 The mixed source concentrations required by the OIB Ce/Tl array can be interpreted as a mantle  
425 ‘background’ that is extremely depleted in Tl, with addition of a material characterised by high Ce and  
426 heterogeneous Tl concentrations, broadly consistent with models of widespread addition of subducted  
427 materials to the mixed OIB source. However, prior to subduction surface materials with high Ce  
428 concentrations (e.g. FeMn sediments) also exhibit elevated Tl concentrations that greatly exceed values that  
429 can be accommodated by the mixing-melting model. If subducted materials are the exotic addition  
430 controlling Ce/Tl systematics in OIB, it is necessary that the majority of Tl must be removed or otherwise

431 lost during subduction processing, rather than being recycled into the deep mantle. A ~20% addition of such  
432 ‘subduction-processed oceanic crust’ (Table 6) to mantle strongly depleted in Tl would produce an  
433 appropriate mixed OIB source.

434 Recently, Shu et al. (2019) analysed the trace element and Tl isotopic composition of a number of eclogites  
435 subducted to a maximum depth of ~90 km before being exhumed, which might represent such ‘subduction-  
436 processed’ oceanic crust. This sample suite has an average Ce concentration of 20  $\mu\text{g/g}$  with an average Tl  
437 concentration of 55 ng/g (Table 6). While the Ce concentration is consistent with the requirements for our  
438 proposed subduction-processed oceanic crust, the Tl concentration is an order of magnitude more than the  
439 maximum we invoke to satisfy our constraints on OIB source concentrations. However, as the eclogite  
440 samples remained within the stability field of Tl-rich phengite, it is likely that further Tl loss would occur  
441 during deeper subduction beyond the phengite stability field.

442 We agree with the findings of Shu et al. (2019) that OIB Ce/Tl systematics indicate widespread incorporation  
443 of subduction-processed oceanic crust into the OIB source, which may consist of (ancient, relatively  
444 enriched) oceanic crust with variable addition of a continental crust component. The Ce/Tl systematics of  
445 OIB thus highlight *similarities*, not differences, between mantle components distinguished by their  
446 radiogenic isotopic compositions. The complete overlap between different lavas representing distinct  
447 (enriched) mantle end-members strongly implies that a high-Ce, low-Tl material such as subduction-  
448 processed oceanic crust is common to OIB sources, and that Tl is near quantitatively removed during  
449 subduction.

#### 450 **4.3 Thallium isotopic composition of OIB**

451 The Tl isotopic composition of the mantle is strikingly homogeneous, and no resolvable Tl isotopic  
452 fractionation is observed during partial melting or fractional crystallisation. Therefore, the significant Tl  
453 isotopic variability observed in global OIB ( $\epsilon^{205}\text{Tl}$  -10.0 to +6.6) requires the addition of isotopically distinct  
454 material to the lavas. The addition of such material can happen in the source, *en route* to the surface, and/or  
455 via subaerial/submarine alteration. We have already argued that alteration does not play a significant role in  
456 the new data, and previous work has similarly screened and discounted altered samples.

457 Thallium isotopic compositions were predicted to covary with the Sr-Nd-Pb radiogenic isotopes used to  
458 classify mantle components, depending on whether AOC or recycled sediments were the primary contributor  
459 of exotic material. However, the elemental systematics of Tl in OIB appear to require highly efficient  
460 removal of Tl during subduction, which potentially weakens the link between deep mantle recycling and OIB  
461 sources in terms of Tl isotopes. Indeed, the first order observation for our global dataset is that primary Tl  
462 isotopic compositions do not co-vary with radiogenic Pb, Sr, Nd, or Hf isotopes (Fig. 7), even within the  
463 chemically diverse Marquesas island group. Although the range is large, the average  $\epsilon^{205}\text{Tl}$  for HIMU and  
464 EM-type lavas overlap within error. For HIMU  $\epsilon^{205}\text{Tl} = -2.6 \pm 6.6$  (2s, n = 37), and for EM  $\epsilon^{205}\text{Tl} = -1.3 \pm 4.4$   
465 (2s, n = 32). The overlap remains even if the comparison is restricted to main-phase St Helena lavas and  
466 EMI-type lavas, for which  $\epsilon^{205}\text{Tl} = -3.2 \pm 3.1$  (2s, n = 10) and  $\epsilon^{205}\text{Tl} = -1.1 \pm 4.0$  (2s, n = 13), respectively.  
467 The absence of correlation between Tl isotopic compositions and Sr-Nd-Pb-Hf radiogenic isotope systems is  
468 consistent with trace element modelling that requires the mantle sources to be ubiquitously depleted in Tl,  
469 likely due to near-quantitative removal of Tl during the subduction process. Elemental parent-daughter pairs  
470 for radiogenic isotopes do not show this same level of depletion in OIB sources, and thus Tl and radiogenic  
471 Sr-Nd-Pb-Hf isotopic compositions can be easily decoupled, as noted by the first study of Tl isotopic  
472 composition in OIB (Nielsen et al. 2006a).

473 However, our finding that Tl isotope systematics may not be a straightforward “fingerprint” of recycled  
474 AOC or FeMn sediment to OIB source regions is at odds with previous work. While no variation in Tl  
475 isotopic composition was found in lavas from the Azores or Iceland (Nielsen et al., 2007), incorporation of  
476 deeply subducted FeMn sediment was invoked to explain variations observed in Hawai’ian picrites (Nielsen  
477 et al., 2006a), and HIMU-type St Helena basalts have been argued to show evidence for incorporation of  
478 subducted AOC (Blusztajn et al., 2018). In the case of Hawai’i, the absence of correlation between Tl stable  
479 and Os radiogenic isotopes was noted, despite the potential for FeMn sediment contributions to control both  
480 systems, and ascribed to the very high Tl/Os ratio such sediments exhibit.

481 Our new data provide a basis for re-evaluating the systematics of Tl isotopes in the HIMU mantle  
482 endmember. The isotopic criterion most commonly used to distinguish HIMU lavas is their radiogenic Pb  
483 isotopic compositions (i.e.  $^{206}\text{Pb}/^{204}\text{Pb} > 19.5$ ), which is commonly interpreted to arise from the subduction of  
484 AOC with high  $^{238}\text{U}/^{204}\text{Pb}$  ratios (‘high  $\mu$ ’), that was isolated in the mantle for 1-2 Ga (e.g. Hofmann and

485 White, 1982; Zindler and Hart, 1986; Chauvel et al., 1992; Stracke et al., 2005). While acknowledging  
486 decoupling of Tl and Sr-Nd-Hf-Pb isotopes, Blusztajn et al. (2018) argue that Tl isotopic compositions that  
487 are generally lighter than those found for MORB combined with Ce/Tl variations provide evidence for the  
488 presence of a recycled upper AOC component in the St Helena source, from which up to 90% of Tl (relative  
489 to Ce) was stripped during subduction processing. Subsequent work investigated eclogites from Cabe  
490 Ortegual and the Raspas Complex, thought to represent the metamorphic equivalents of altered oceanic crust  
491 (Shu et al., 2019). The eclogites have a similar range in Tl isotopic compositions as the main phase St.  
492 Helena lavas ( $\epsilon^{205}\text{Tl} \approx -5.5$  to  $-1.0$ ), and thus Shu et al. (2019) proposed a genetic link between the two.

493 This interpretation is complicated by the observation that, for the full OIB dataset (Fig. 8), the majority of  
494 HIMU samples have  $\epsilon^{205}\text{Tl}$  values that overlap with the range of results obtained for EM-type samples ( $\epsilon^{205}\text{Tl}$   
495  $\geq -6.5$ ; Fig. 8b, 8d). In addition, there is no convincing co-variation of  $\epsilon^{205}\text{Tl}$  with Ce/Tl and Ce/Pb for either  
496 St Helena lavas (Fig. 8a, 8c) or the complete OIB dataset, with EM-type samples again overlapping the  
497 whole range of HIMU-type lavas. While one HIMU-type lava does exhibit the lightest reported Tl isotopic  
498 composition of any OIB sampled to date ( $\epsilon^{205}\text{Tl} \approx -10$ ), the broad overlap in  $\epsilon^{205}\text{Tl}$  for HIMU- and EM-type  
499 OIB does not provide a clear distinction between different mantle end-members based on Tl isotopic  
500 compositions alone. It therefore appears that Tl isotopic compositions are decoupled not just from radiogenic  
501 isotopes and Tl concentrations, as suggested by Shu et al. (2019), but also – at least on a global scale – from  
502 incompatible trace element ratios held to be indicative of AOC contributions.

503 We concur with the conclusion of Blusztajn et al. (2018) that the Ce/Tl ratios of OIB appear to be broadly  
504 complementary to those found in island arc lavas. It is therefore necessary to explain *how* Tl isotopic  
505 systematics become (apparently) decoupled from Tl elemental systematics. Fitting our model to elemental  
506 systematics data requires highly efficient ( $\sim 99\%$ , relative to Ce) removal of Tl from heterogeneous  
507 subducting materials, with only a small proportion of subducted Tl returned to OIB source regions in the  
508 deep mantle. Therefore, the low Tl concentrations of the OIB sources produce magmas with Tl signatures  
509 that can be readily overprinted by addition of isotopically distinct material.

510 The notion that Tl isotopic compositions distinct from mantle values are due to the input of Tl-rich,  
511 isotopically distinct materials can be further examined via the magnitude of the negative Tl concentration  
512 anomaly observed for OIB relative to geochemically similar elements. When the magnitude of the Tl

513 anomaly  $Tl/Tl^*$  (see caption to Figure 9) is plotted against Tl isotopic composition, samples with  $Tl/Tl^* >$   
514  $\sim 0.5$  (calculated relative to Cs and Rb) generally have Tl isotopic compositions that differ from the mantle  
515 (Fig. 9a, 9b). As would be expected given the decoupling of Tl and radiogenic isotopic compositions, this  
516 pattern is not restricted to or consistent within any one radiogenic isotope end-member, and some samples  
517 with  $Tl/Tl^* < \sim 0.5$  also display non-mantle values. Ruling out post-depositional isotopic effects, the question  
518 that arises is where does the addition of material with non-mantle Tl isotopic compositions take place? The  
519 mantle source or *en route* to eruption?

520 Addition of isotopically distinct Tl to the OIB source via residual Tl from a subduction-processed slab and/or  
521 addition during ascent through the crust via assimilation of country rock, including sediments and  
522 previously-erupted and subsequently altered lavas are both reasonable processes. For example, variation in  
523 the extent and type of material assimilated during different stages of magmatism might account for the  
524 distinct average Tl isotopic compositions observed by Blusztajn et al. (2018) for St Helena early-, main-, and  
525 late-stage lavas. Given the Tl concentration contrast between magma and potential inputs, neither origin for  
526 Tl isotope variations – source heterogeneity or assimilation – would necessarily cause resolvable changes to  
527 other geochemical markers (e.g. model of Nielsen et al., 2006a; Fig. S6). Caution is therefore advisable when  
528 interpreting Tl isotopic compositions of OIB as a direct reflection of the mantle source. However, there is the  
529 potential that variable crustal assimilation of isotopically distinct Tl might be identifiable in high resolution  
530 studies of lavas from individual volcanic edifices, yielding insight into their magmatic plumbing architecture.

## 531 **5. Conclusions**

532 Fresh lavas from divergent, convergent and intraplate settings can be distinguished by their distinct  
533 systematics in plots of Ce/Tl versus Tl concentrations. The observed patterns can be reproduced by models  
534 of fractional, non-modal melting, providing insights into the cycling of Tl through the mantle. The Ce/Tl  
535 systematics of MORB can be reproduced by the combined effects of different extents of partial melting and  
536 variations in  $D_{\text{cpx/melt}}^{\text{Ce}}$  and initial Tl and Ce concentrations, without a significant role for sulfides. In contrast,  
537 the Ce/Tl systematics of OIB cannot be generated from a primitive mantle source, but instead require a  
538 source that is markedly depleted in Tl ( $< 1$  ng/g) prior to addition of exotic thallium. The requirement for Tl-  
539 depleted OIB source regions is consistent with mounting evidence that the extent of present day mantle  
540 depletion may be underestimated (e.g. Stracke, 2012; Stracke et al., 2011, 2019; Salters et al., 2011; Salters

541 and Dick, 2002; Cipriani et al., 2004; Sanfillippo et al., 2019). The OIB array can be generated from a  
542 depleted mantle source with addition of up to 20% subducted material from which >99% of Tl has been  
543 stripped during subduction processing. This suggests that Tl constitutes an extreme example of the behaviour  
544 of fluid-mobile elements in subduction zone settings, such that co-variations of Tl with other elements may  
545 further constrain elemental subduction zone cycling.

546 Thallium and radiogenic isotopic compositions are decoupled, and Tl isotopic compositions cannot be used  
547 in isolation to distinguish between continental and oceanic crust contribution to OIB source regions. The  
548 observed decoupling of Tl and radiogenic isotopic compositions most likely reflects (1) the sensitivity of Tl  
549 to small variations in the isotopic composition of residual Tl, and/or (2) the extreme Tl concentration contrast  
550 between mantle and surface materials. Despite the lack of co-variation with radiogenic isotopes, global OIB  
551 display a significant range in primary Tl isotopic compositions which must reflect addition of isotopically  
552 distinct material. However, where this Tl addition takes place remains ambiguous. The potential  
553 incorporation of Tl-rich materials at crustal levels during magma ascent is a feasible alternative interpretation  
554 to the generation of Tl isotopic variability due to incorporation of residual slab-derived Tl at mantle depths  
555 following subduction processing.

## 556 **Acknowledgements**

557 AB was funded by an Imperial College London Earth Science and Engineering Janet Watson departmental  
558 PhD scholarship with all analytical costs covered by start-up funds to JP. We thank Barry Coles and  
559 Katharina Kreissig for keeping the MAGIC instruments and clean labs running smoothly. CC was supported  
560 in part by ERC project SHRED (project 833632), and this is contribution 4149 of the IPGP. We appreciate  
561 the comments of Folkmar Hauff, Kevin Konrad, four anonymous reviewers, and the editorial handling of  
562 James Day, all of which helped improve the manuscript.

## 563 **Appendix**

### 564 **I. Elemental concentrations**

565 **MORB.** For Ce concentration, we use the values of Workman and Hart (2005) for Depleted MORB Mantle  
566 (DMM), Enriched MORB Mantle (EMM), and the average MORB source. For Tl concentration, we consider  
567 previous DMM estimates along with values that provide the best fit for our model.

568 **OIB.** We used the values of McDonough and Sun (1995) as our initial values for PM, then varied  
569 concentrations as required to fit our model to the data.

## 570 **II. Thallium partitioning**

571 **Chalcophilia.** Nielsen et al. (2014) based their values of  $D_{\text{sulf/sil}}^{\text{Tl}}$  during MORB melting (18–100) on data  
572 from Kiseeva and Wood (2013), who reported  $D_{\text{sulf/sil}}^{\text{Tl}} = 4\text{--}24$ . However, a growing body of evidence  
573 supports the concept that “mixed affinity” behaviour is exhibited by Tl, i.e. elemental behaviour cannot be  
574 described as either predominantly chalcophile or predominantly lithophile.

575 Kiseeva and Wood (2015) report  $D_{\text{sulf/sil}}^{\text{Tl}}$  of 4–33, and note that “partitioning of most elements is a strong  
576 function of the oxygen (or FeO) content of the sulphide”, which “increases linearly with the FeO content of  
577 the silicate melt and decreases with the Ni content of the sulphide.” Wood and Kiseeva (2015) go on to state  
578 that Tl partitioning does not obey this simple model, nor one extended through consideration of additional  
579 parameters: “Despite simple and predictable partitioning behavior for many elements, several important  
580 elements (Ni, Cu, Ag, Mn, Tl) show strongly non-linear dependences of  $\log D_i$  on  $\log[\text{FeO}]$  and we were  
581 unable to assign them to any one particular category in terms of affinity for sulfide.”

582 Jenner (2017) calculated that for typical MORB melting  $D_{\text{sulf/sil}}^{\text{Tl}} = 7$ ; Greaney et al. (2017) observe mixed  
583 affinity behaviour during magmatic differentiation at Kilauea Iki. Wang et al. (2018) suggested that a  
584 significant proportion of the Tl contents of peridotites are hosted in interstitial late-crystallising silicate  
585 phases, finding that sulphides typically contribute <30% of the bulk rock Tl budget. These observations are  
586 consistent with poor correlation of Tl concentrations with chalcophile element concentrations in most  
587 igneous contexts (e.g. Prytulak et al., 2017).

588 **Silicate minerals.** Although Tl is known to be highly incompatible, partitioning of Tl between silicate  
589 minerals and melt remains poorly constrained. Nielsen et al. (2014) therefore assumed  $D_{\text{min/melt}}^{\text{Tl}}$  identical to  
590  $D_{\text{min/melt}}^{\text{Rb}}$  due to the similarity in ionic charge and radius.  $\text{Tl}^+$  is well-known to substitute for  $\text{K}^+$  in silicate  
591 minerals (e.g. Shaw et al 1952), as documented by e.g. Rader et al. (2018), and we also assume similar  
592 partitioning behaviour of Rb and Tl in silicate contexts.

## 593 **III. Cerium partitioning**

594 Although variation in mineral-melt partitioning of Ce between clinopyroxene and basaltic melt (herein  
595  $D_{\text{cpx/melt}}^{\text{Ce}}$ ) is not required to model the MORB Ce/Tl array, it is likely that such variation does exist and does  
596 contribute to the observed pattern. The GERM database (as of June 2020) documents a total range in  
597  $D_{\text{cpx/melt}}^{\text{Ce}}$  from 0.017 (Frey, 1969) to 0.82 (Vannucci et al., 1998), excluding the values of Nagasawa (1973),  
598 which were determined on natural samples showing signs of significant alteration (Uchimizu, 1966).  
599  $D_{\text{cpx/melt}}^{\text{Ce}}$  is generally observed to increase with increasing Wollastonite and tetrahedrally-coordinated Al  
600 content of clinopyroxene. The data compilation of Sun and Liang (2012) features a range of  $D_{\text{cpx/melt}}^{\text{Ce}}$  from  
601 0.019 (Salters and Longhi, 1999) to 0.27 (Gaetani and Grove, 1995), excluding the data of Wood and Trigila  
602 (2001) determined for highly potassic melts ( $D_{\text{cpx/melt}}^{\text{Ce}}$  from 0.48 to 1.31). This information is presented  
603 graphically in Figure A1.

604 Johnston and Schwab (2004) additionally determined a  $D_{\text{cpx/melt}}^{\text{Ce}}$  value of 0.47 during experiments on the  
605 partial melting of peridotite (not shown). Further data for partitioning of REE in the presence of high-Ca  
606 clinopyroxenes was compiled by Bédard (2014), though the dataset for terrestrial basalts is limited.

607 While Sun and Liang (2012) provided recommended values for  $D_{\text{cpx/melt}}^{\text{Ce}}$  during MORB melting, they note  
608 that these values are based on highly simplified thermodynamic models of clinopyroxene that may represent  
609 unrealistically restricted mineral composition ranges. We therefore explore a range of  $D_{\text{cpx/melt}}^{\text{Ce}}$  from 0.01 to  
610 0.8 in our modelling. We do not consider 0.8 a value that is *likely* to be achieved in natural rocks, but it is  
611 informative as an end-member scenario.

## 612 **References**

- 613 Adam J. and Green T. (2006) Trace-element partitioning between mica- and amphibole-bearing garnet lherzolite and  
614 hydrous basaltic melt: 1. Experimental results and the investigation of controls on partitioning behaviour. *Contrib.*  
615 *Mineral. Petrol.* **152**, 1–17. doi:10.1007/s00410-006-0085-4
- 616 Bach W., Erzinger J., Alt J. C. and Teagle D. A. H. (1996) 4. Chemistry of the lower sheeted dike complex, Hole 504B  
617 (Leg 148): influence of magmatic differentiation and hydrothermal alteration. *Proc. ODP Sci. Results* **148**, 39–55.
- 618 Baker M.B. and Stolper E.M. (1994) Determining the composition of high-pressure mantle melts using diamond  
619 aggregates. *Geochim. Cosmochim. Acta* **58**, 2811–2827. doi:10.1016/0016-7037(94)90116-3
- 620 Baker R. G. A., Rehkämper M., Hinkley T. K., Nielsen S. G. and Toutain J. P. (2009) Investigation of thallium fluxes  
621 from subaerial volcanism—Implications for the present and past mass balance of thallium in the oceans. *Geochim.*  
622 *Cosmochim. Acta* **73**, 6340–6359. doi:10.1016/j.gca.2009.07.014

- 623 Bebout, G. E. (2007) Metamorphic chemical geodynamics of subduction zones. *Earth Planet. Sci. Lett.* **260**, 373–393.  
624 doi:10.1016/j.epsl.2007.05.050
- 625 Bédard J. H. (2013) Parameterizations of calcic clinopyroxene—melt trace element partition coefficients. *Geochem.*  
626 *Geophys. Geosys.* **15**, 303–336. doi:10.1002/2013GC005112
- 627 Blundy J. D., Robinson J. A. C. and Wood B. J. (1998) Heavy REE are compatible in clinopyroxene on the spinel  
628 lherzolite solidus. *Earth Planet. Sci. Lett.* **160**, 493–504. doi:10.1016/S0012-821X(98)00106-X
- 629 Blusztajn J., Nielsen S. G., Marschall H. R., Shu Y., Ostrander C. M. and Hanyu T. (2018) Thallium isotope  
630 systematics in volcanic rocks from St Helena - constraints on the origin of the HIMU reservoir. *Chem. Geol.* **476**,  
631 292–301. doi:10.1016/j.chemgeo.2017.11.025
- 632 Bo T., Katz R. F., Shorttle O. and Rudge, J. F. (2018) The melting column as a filter of mantle trace-element  
633 Heterogeneity. *Geochem. Geophys. Geosyst.* **19**, 4694–4721. doi:10.1029/2018GC007880
- 634 Brett E. K. A., Prytulak J., Hammond S. J. and Rehkämper M. (2018). Thallium concentration and stable isotope  
635 compositions of sixteen international reference materials. *Geostand. Geoanal. Res.* **42**, 339–360.  
636 doi:10.1111/ggr.12215
- 637 Chauvel C., Hofmann A. W. and Vidal P. (1992) HIMU-EM: The French Polynesian connection. *Earth Planet. Sci.*  
638 *Lett.* **110**, 99–119. doi:10.1016/0012-821X(92)90042-T
- 639 Chauvel C., McDonough W., Guille G., Maury R. and Duncan R. (1997) Contrasting old and young volcanism in  
640 Rurutu Island, Austral chain. *Chem. Geol.* **139**, 125–143. doi:10.1016/S0009-2541(97)00029-6
- 641 Chauvel C., Maury R. C., Blais S., Lewin E., Guillou H., Guille G., Rossi P. and Gutscher M. A. (2012) The size of  
642 plume heterogeneities constrained by Marquesas isotopic stripes. *Geochem. Geophys. Geosyst.* **13**, Q07005.  
643 doi:10.1029/2012GC004123
- 644 Cipriani A., Brueckner H. K., Bonatti E. and Brunelli D. (2004) Oceanic crust generated by elusive parents: Sr and Nd  
645 isotopes in basalt-peridotite pairs from the Mid-Atlantic Ridge. *Geology* **32**, 657–660. doi:10.1130/G20560.1
- 646 Coggon R. M., Rehkämper M., Atteck C., Teagle D. A. H., Alt J. C. and Cooper M. J. (2014) Controls on thallium  
647 uptake during hydrothermal alteration of the upper ocean crust. *Geochim. Cosmochim. Acta* **144**, 25–42.  
648 doi:10.1016/j.gca.2014.09.001
- 649 Cox D., Watt S. F. L., Jenner F. E., Hastie A. R. and Hammond S. J. (2019) Chalcophile element processing beneath a  
650 continental arc stratovolcano. *Earth Planet. Sci. Lett.* **522**, 1–11. doi:10.1016/j.epsl.2019.06.017
- 651 Ding S. and Dasgupta R. (2018) Sulfur inventory of Ocean Island Basalt source regions constrained by modeling the  
652 fate of sulfide during decompression melting of a heterogeneous mantle. *J. Petrol.* **59**, 1281–1308.  
653 doi:10.1093/petrology/egy061
- 654 Donnelly K. E., Goldstein S. L., Langmuir C. H. and Spiegelman M. (2004) Origin of enriched ocean ridge basalts and  
655 implications for mantle dynamics. *Earth Planet. Sci. Lett.* **226**, 347–366. doi:10.1016/j.epsl.2004.07.019
- 656 Dupuy C., Fratta M. and Shaw D. M. (1973) Partition coefficient of thallium compared with rubidium. *Earth Planet.*  
657 *Sci. Lett.* **19**, 209–212. doi:10.1016/0012-821X(73)90116-7

- 658 Eggins S. M., Woodhead J. D., Kinsley L. P. J., Mortimer G. E., Sylvester P., McCulloch M. T. Hergt J. M. and  
659 Handler M. R. (1997) A simple method for the precise determination of  $\geq 40$  trace elements in geological samples  
660 by ICPMS using enriched isotope internal standardisation. *Chem. Geol.* **134**, 311–326. doi:10.1016/S0009-  
661 2541(96)00100-3
- 662 Elliott T., Blichert-Toft J., Heumann A., Koetsier G. and Forjaz V. (2007) The origin of enriched mantle beneath São  
663 Miguel, Azores. *Geochim. Cosmochim. Acta* **71**, 219–240. doi:10.1016/j.gca.2006.07.043
- 664 Fitzpayne A., Prytulak J., Giuliani A. and Hergt J. (2020) Thallium isotopic composition of phlogopite in kimberlite-  
665 hosted MARID and PIC mantle xenoliths. *Chem. Geol.* **531**, 119347. doi:10.1016/j.chemgeo.2019.119347
- 666 Frey F. A. (1969) Rare earth abundances in a high-temperature peridotite intrusion. *Geochim. Cosmochim. Acta* **33**,  
667 1429–1447. doi:10.1016/0016-7037(69)90183-5
- 668 Gaetani G. A. and Grove T. L. (1995) Partitioning of rare earth elements between clinopyroxene and silicate melt:  
669 crystal-chemical controls. *Geochim. Cosmochim. Acta* **59**, 1951–1962. doi:10.1016/0016-7037(95)00119-0
- 670 Gaetani G. A., Kent A., Grove T. L., Hutchenson I. and Stolper E. M. (2003) Mineral/melt partitioning of trace  
671 elements during hydrous peridotite partial melting. *Contrib. Mineral. Petrol.* **145**, 391–405. doi:10.1016/0016-  
672 7037(95)00119-0
- 673 Gale A., Dalton C. A., Langmuir C. H., Su Y., Schilling J. G. (2013) The mean composition of ocean ridge basalts.  
674 *Geochem. Geophys. Geosyst.* **14**, 489–518. doi:10.1029/2012GC004334
- 675 Greaney A. T., Rudnick R. L., Helz R. T., Gaschnig R. M., Piccoli P. M. and Ash R. D. (2017) The behavior of  
676 chalcophile elements during magmatic differentiation as observed in Kilauea Iki lava lake, Hawaii. *Geochim.*  
677 *Cosmochim. Acta* **210**, 71–96. doi:10.1016/j.gca.2017.04.033
- 678 Green T. H., Blundy J. D., Adam J. and Yaxley G. M. (2000) SIMS determination of trace element partition coefficients  
679 between garnet, clinopyroxene, and hydrous basaltic liquids at 2–7.5 GPa and 1080–1200°C. *Lithos* **53**, 165–187.  
680 doi:10.1016/S0024-4937(00)00023-2
- 681 Hauri E. H., Wagner T. P. and Grove T. L. (1994) Experimental and natural partitioning of Th-U-Pb and other trace  
682 elements between garnet, clinopyroxene and basaltic melts. *Chem. Geol.* **117**, 149–166. doi:10.1016/0009-  
683 2541(94)90126-0
- 684 Heinrichs H., Schulz-Dobrick B. and Wedepohl K. H. (1980) Terrestrial geochemistry of Cd, Bi, Tl, Pb, Zn and Rb.  
685 *Geochim. Cosmochim. Acta* **44**, 1519–1533. doi:10.1016/0016-7037(80)90116-7
- 686 Hill E., Wood B. J. and Blundy J. D. (2000) The effect of Ca-Tschermaks component on trace element partitioning  
687 between clinopyroxene and silicate melt. *Lithos* **53**, 205–217. doi:10.1016/S0024-4937(00)00025-6
- 688 Hofmann A. W. (1997) Mantle geochemistry: the message from oceanic volcanism. *Nature* **385**, 219–229.  
689 doi:10.1038/385219a0
- 690 Hofmann A. W. and White W. M. (1982) Mantle plumes from ancient oceanic crust. *Earth Planet. Sci. Lett.* **57**, 421–  
691 436. doi:10.1016/0012-821X(82)90161-3

692 Irving A. J. and Frey F. A. (1984) Trace element abundances in megacrysts and their host basalts: constraints on  
693 partition coefficients and megacryst genesis. *Geochim. Cosmochim. Acta* **48**, 1201–1221. doi:10.1016/0016-  
694 7037(84)90056-5

695 Jenner F. E. (2017) Cumulate causes for the low contents of sulfide-loving elements in the continental crust. *Nat.*  
696 *Geosci.* **10**, 524–529. doi:10.1038/ngeo2965

697 Jenner F. and O'Neill H. St. C. (2012). Analysis of 60 elements in 616 ocean floor basaltic glasses. *Geochem. Geophys.*  
698 *Geosyst.* **13**, Q02005. doi:10.1029/2011GC004009

699 Johnson K. T. M. (1998) Experimental determination of partition coefficients for rare earth and high-field-strength  
700 elements between clinopyroxene, garnet, and basaltic melt at high pressures. *Contrib. Mineral. Petrol.* **133**, 60–68.  
701 doi:10.1007/s004100050437

702 Johnston A. D. and Schwab B. E. (2004) Constraints on clinopyroxene/melt partitioning of REE, Rb, Sr, Ti, Cr, Zr, and  
703 Nb during mantle melting: first insights from direct peridotite melting experiments at 1.0 GPa. *Geochim.*  
704 *Cosmochim. Acta* **68**, 4949–4962. doi:10.1016/j.gca.2004.06.009

705 Kiseeva E. S. and Wood B. J. (2013) A simple model for chalcophile element partitioning between sulphide and silicate  
706 liquids with geochemical applications. *Earth Planet. Sci. Lett.* **383**, 68–81. doi:10.1016/j.epsl.2013.09.034

707 Kiseeva E. S. and Wood B. J. (2015) The effects of composition and temperature on chalcophile and lithophile element  
708 partitioning into magmatic sulphides. *Earth Planet. Sci. Lett.* **424**, 280–294. doi:10.1016/j.epsl.2015.05.012

709 Klemme S., Blundy J. D. and Wood B. J. (2002) Experimental constraints on major and trace element partitioning  
710 during partial melting of eclogite. *Geochim. Cosmochim. Acta* **66**, 3109–3123. doi:10.1016/S0016-7037(02)00859-1

711 Liu Y., Samaha N.-T. and Baker D. R. (2007) Sulfur concentration at sulfide saturation (SCSS) in magmatic silicate  
712 melts. *Geochim. Cosmochim. Acta* **71**, 1783–1799. doi:10.1016/j.gca.2007.01.004

713 Liu B. and Liang Y. (2020) Importance of the size and distribution of chemical heterogeneities in the mantle source to  
714 the variations of isotope ratios and trace element abundances in mid-ocean ridge basalts. *Geochim. Cosmochim.*  
715 *Acta* **268**, 383–404. doi:10.1016/j.gca.2019.10.013

716 Matsui Y., Onuma N., Nagasawa H., Higuchi H. and Banno S. (1977) Crystal structure control in trace element  
717 partitioning between crystal and magma. *Tectonics* **100**, 315-324.

718 Mavrogenes J. A. and O'Neill H. St. C. (1999) The relative effects of pressure, temperature and oxygen fugacity on the  
719 solubility of sulfide in mafic magmas. *Geochim. Cosmochim. Acta* **63**, 1173–1180. doi:10.1016/S0016-  
720 7037(98)00289-0

721 McDade P., Blundy J. D. and Wood B. J. (2003a) Trace element partitioning on the Tinaquillo Lherzolite solidus at 1.5  
722 GPa. *Phys. Earth Planet. Int.* **139**, 129–147. doi:10.1016/S0031-9201(03)00149-3

723 McDade P., Blundy J. D. and Wood B.J. (2003b) Trace element partitioning between mantle wedge peridotite and  
724 hydrous MgO-rich melt. *Am Mineral.* **88**, 1825–1831. doi:10.2138/am-2003-11-1225

725 McDonough W. F. and Sun S.-s. (1995) The composition of the earth. *Chem. Geol.* **120**, 223–253. doi:10.1016/0009-  
726 2541(94)00140-4

- 727 Minster J. F. and Allègre C. J. (1978) Systematic use of trace elements in igneous processes. *Contrib. Mineral. Petrol.*  
728 **68**, 37–52. doi:10.1007/BF00375445
- 729 Montelli R., Nolet G., Dahlen F. A. and Masters G. (2006) A catalogue of deep mantle plumes: New results from finite-  
730 frequency tomography. *Geochem. Geophys. Geosyst.* **7**, Q11007. doi:10.1029/2006GC001248
- 731 Morgan W. J. (1971) Convection plumes in the lower mantle. *Nature* **230**, 42–43. doi:10.1038/230042a0
- 732 Nagasawa H., Wakita H., Higuchi H. and Onuma N. (1969) Rare Earths in peridotite nodules: an explanation of the  
733 genetic relationship between basalt and peridotite nodules. *Earth Planet. Sci. Lett.* **5**, 377–381. doi:10.1016/S0012-  
734 821X(68)80067-6
- 735 Nagasawa H. (1973). Rare-Earth distribution in alkali rocks from Oki-Dogo Island, Japan. *Contrib. Mineral. Petrol.* **39**,  
736 301–308. doi:10.1007/BF00376470
- 737 Nielsen S. G., Rehkämper M., Baker J. and Halliday A. N. (2004) The precise and accurate determination of thallium  
738 isotope compositions and concentrations for water samples by MC-ICPMS. *Chem. Geol.* **204**, 109–124.  
739 doi:10.1016/j.chemgeo.2003.11.006
- 740 Nielsen S. G., Rehkämper M., Porcelli D., Andersson P., Halliday A. N., Swarzenski P. W., Latkoczy C. and Günther  
741 D. (2005) Thallium isotope composition of the upper continental crust and rivers – an investigation of the  
742 continental sources of dissolved marine thallium. *Geochim. Cosmochim. Acta* **19**, 2007–2019.  
743 doi:10.1016/j.gca.2004.10.025
- 744 Nielsen S. G., Rehkämper M., Norman M. D., Halliday A. N. and Harrison D. (2006a). Thallium isotopic evidence for  
745 ferromanganese sediments in the mantle source of Hawaiian basalts. *Nature* **439**, 314–317.  
746 doi:10.1038/nature04450
- 747 Nielsen S. G., Rehkämper M., Teagle D. A. H., Butterfield D. A., Alt J. C. and Halliday A. N. (2006b) Hydrothermal  
748 fluid fluxes calculated from the isotopic mass balance of thallium in the ocean crust. *Earth Planet. Sci. Lett.* **251**,  
749 120–133. doi:10.1016/j.epsl.2006.09.002
- 750 Nielsen S. G., Rehkämper M., Brandon A. D., Norman M. D., Turner S. and O'Reilly S. Y. (2007) Thallium isotopes in  
751 Iceland and Azores lavas – implications for the role of altered crust and mantle geochemistry. *Earth Planet. Sci.*  
752 *Lett.* **264**, 332–345. doi:10.1016/j.epsl.2007.10.008
- 753 Nielsen S.G., Wasylenki L. E., Rehkämper M., Peacock C. L., Xue Z. and Moon E. M. (2013) Towards an  
754 understanding of thallium isotope fractionation during adsorption to manganese oxides. *Geochim. Cosmochim. Acta*  
755 **117**, 252–265. doi:10.1016/j.gca.2013.05.004
- 756 Nielsen S. G., Shimizu N., Lee C. T. A. and Behn M. D. (2014) Chalcophile behaviour of thallium during MORB  
757 melting and implications for the sulfur content of the mantle. *Geochem. Geophys. Geosyst.* **15**, 4905–4919.  
758 doi:10.1002/2014GC005536
- 759 Nielsen S. G., Klein F., Kading T., Blusztajn J. and Wickham K. (2015). Thallium as a tracer of fluid-rock interaction in  
760 the shallow Mariana forearc. *Earth Planet. Sci. Lett.* **430**, 416–426. doi:10.1016/j.epsl.2015.09.001

- 761 Nielsen S. G., Yagodinski G., Prytulak J., Plank T., Kay S. M., Kay R. W., Blusztajn J., Owens J. D., Auro M. and  
762 Kading T. (2016) Tracking along-arc sediment inputs to the Aleutian arc using thallium isotopes. *Geochim.*  
763 *Cosmochim. Acta* **181**, 217–237. doi:10.1016/j.gca.2016.03.010
- 764 Nielsen S.G., Prytulak J., Blusztajn J., Shu Y., Auro M., Regelous M. and Walker J. (2017a) Thallium isotopes as  
765 tracers of recycled materials in subduction zones: review and new data for lavas from Tonga-Kermadec and Central  
766 America. *J. Vol. Geotherm. Res.* **339**, 23–40. doi:10.1016/j.jvolgeores.2017.04.024
- 767 Nielsen S. G., Prytulak J. and Rehkämper M. (2017b) Investigation and application of thallium isotope fractionation.  
768 *Rev. Mineral. Geochem.* **82**, 799–850. doi:10.2138/rmg.2017.82.18
- 769 O'Neill H. St. C. and Mavrogenes J. A. (2002) The sulfide capacity and the sulfur content at sulfide saturation of  
770 silicate melts at 1400°C and 1 bar. *J. Petrol.* **43**, 1049–1087. doi:10.1093/petrology/43.6.1049
- 771 Palme H. and O'Neill H. St. C. (2014) Cosmochemical Estimates of Mantle Composition. In *The Mantle and Core 2*  
772 (eds. D. H. Heinrich and K. T. Karl). Elsevier, Amsterdam. pp. 1-38.
- 773 Peacock C. L. and Moon E. M. (2012) Oxidative scavenging of thallium by birnessite: explanation for thallium  
774 enrichment and stable isotope fractionation in marine ferromanganese precipitates. *Geochim. Cosmochim. Acta* **84**,  
775 297–313. doi:10.1016/j.gca.2012.01.036
- 776 Piper D. Z. (1974) Rare earth elements in ferromanganese nodules and other marine phases. *Geochim. Cosmochim. Acta*  
777 **38**, 1007–1022. doi:10.1016/0016-7037(74)90002-7
- 778 Prytulak J., Nielsen S. G., Plank T., Barker M. and Elliott T. (2013). Assessing the utility of thallium and thallium  
779 isotopes for tracing subduction zone inputs to the Mariana arc. *Chem. Geol.* **345**, 129–149.  
780 doi:10.1016/j.chemgeo.2013.03.003
- 781 Prytulak J., Brett E. K. A., Webb M., Rehkämper M., Plank T., Savage P.S. and Woodhead J. (2017) Thallium  
782 elemental behavior and stable isotope fractionation during magmatic processes. *Chem. Geol.* **448**, 71–83.  
783 doi:10.1016/j.chemgeo.2016.11.007
- 784 Rader S. T., Mazdab F. K. and Barton M. D. (2018) Mineralogical thallium geochemistry and isotope variations from  
785 igneous, metamorphic, and metasomatic systems. *Geochim. Cosmochim. Acta* **243**, 42–65.  
786 doi:10.1016/j.gca.2018.09.019
- 787 Reed, B.C. (2010) A spreadsheet for linear least-squares fitting with errors in both coordinates. *Phys. Ed.* **45**, 93–96.  
788 doi:10.1088/0031-9120/45/1/011
- 789 Rehkämper M. and Halliday A. N. (1999) The precise measurement of Tl isotopic compositions by MC-ICPMS:  
790 application to the analysis of geological materials and meteorites. *Geochim. Cosmochim. Acta* **63**, 935-944.  
791 doi:10.1016/S0016-7037(98)00312-3
- 792 Rehkämper M., Frank M., Hein J. R., Porcelli D., Halliday A., Ingri J. and Liebetrau V. (2002) Thallium isotope  
793 variations in seawater and hydrogenetic, diagenetic, and hydrothermal ferromanganese deposits. *Earth Planet. Sci.*  
794 *Lett.* **197**, 65–81. doi:10.1016/S0012-821X(02)00462-4
- 795 Rehkämper M. and Nielsen S. G. (2004) The mass balance of dissolved thallium in the oceans. *Mar. Chem.* **85**, 125–  
796 139. doi:10.1016/j.marchem.2003.09.006

797 Rudge J. F., MacLennan J. and Stracke A. (2013) The geochemical consequences of mixing melts from a heterogeneous  
798 mantle. *Geochim. Cosmochim. Acta* **114**, 112–143. doi:10.1016/j.gca.2013.03.042

799 Salters V. J. M. and Dick H. J. B. (2002) Mineralogy of the mid-ocean-ridge basalt source from neodymium isotopic  
800 composition of abyssal peridotites. *Nature* **418**, 68–72. doi:10.1038/nature00798

801 Salters V. J. M. and Longhi J. (1999) Trace element partitioning during the initial stages of melting beneath mid-ocean  
802 ridges. *Earth Planet. Sci. Lett.* **166**, 15–30. doi:10.1016/S0012-821X(98)00271-4

803 Salters V. J. M. and Stracke A. (2004) Composition of the depleted mantle. *Geochem. Geophys. Geosyst.* **5**, Q05B07.  
804 doi:10.1029/2003GC000597

805 Salters V. J. M., Mallick S., Hart S. R., Langmuir C. H. and Stracke A. (2011) Domains of depleted mantle: new  
806 evidence from hafnium and neodymium isotopes. *Geochem. Geophys. Geosyst.* **12**, Q08001.  
807 doi:10.1029/2011GC003617

808 Sanfillippo A., Salters V., Tribuzio R. and Zanetti A. (2019) Role of ancient, ultra-depleted mantle in mid-ocean-ridge  
809 magmatism. *Earth Planet. Sci. Lett.* **511**, 89–98. doi:10.1016/j.epsl.2019.01.018

810 Shaw D. M. (1952) The geochemistry of thallium. *Geochim. Cosmochim. Acta* **2**, 118–154. doi:10.1016/0016-  
811 7037(52)90003-3

812 Shu Y., Nielsen S. G., Zeng Z., Shinjo R., Blusztajn J., Wang X. and Chen S. (2017) Tracing subducted sediment inputs  
813 to the Ryukyu Arc-Okinawa Trough system: evidence from thallium isotopes. *Geochim. Cosmochim. Acta* **217**,  
814 462–491. doi:10.1016/j.gca.2017.08.035

815 Shu Y., Nielsen S. G., Marschall H. R., John T., Blusztajn J. and Auro M. (2019) Closing the loop: subducted eclogites  
816 match thallium isotope compositions of ocean island basalts. *Geochim. Cosmochim. Acta* **250**, 130–148.  
817 doi:10.1016/j.gca.2019.02.004

818 Sims K. W. W. and DePaolo D. J. (1997) Inferences about mantle magma sources from incompatible element  
819 concentration ratios in oceanic basalts. *Geochim. Cosmochim. Acta* **61**, 765–784. doi:10.1016/S0016-  
820 7037(96)00372-9

821 Sparks J. W. (1995) 7. Geochemistry of the lower sheeted dyke complex, Hole 504B, Leg 140. *Proc. ODP Sci. Results*  
822 **137**, 81–97.

823 Stracke A. (2012) Earth's heterogeneous mantle: a product of convection-driven interaction between crust and mantle.  
824 *Chem. Geol.* **330-331**, 274–299. doi:10.1016/j.chemgeo.2012.08.007

825 Stracke A. and Bourdon B. (2009) The importance of melt extraction for tracing mantle heterogeneity. *Geochim.*  
826 *Cosmochim. Acta* **73**, 218–238. doi:10.1016/j.gca.2008.10.015

827 Stracke A., Bizimis M. and Salters V. J. M. (2003). Recycling oceanic crust: Quantitative constraints. *Geochem.*  
828 *Geophys. Geosyst.* **4**, Q08003. doi:10.1029/2001GC000223

829 Stracke A., Hofmann A. W. and Hart S. R. (2005) FOZO, HIMU, and the rest of the mantle zoo. *Geochem. Geophys.*  
830 *Geosyst.* **6**, Q05007. doi:10.1029/2004GC000824

- 831 Stracke A., Snow J. E., Hellebrand E., von der Handt A., Bourdon B., Birbaun K. and Günther D. (2011) Abyssal  
832 peridotite Hf isotopes identify extreme mantle depletion. *Earth Planet. Sci. Lett.* **308**, 359–368.  
833 doi:10.1016/j.epsl.2011.06.012
- 834 Stracke A., Genske F., Berndt J. and Koornneef J. M. (2019) Ubiquitous ultra-depleted domains in Earth's mantle. *Nat.*  
835 *Geosci.* **12**, 851–855. doi:10.1038/s41561-019-0446-z
- 836 Sun C. and Liang Y. (2012) Distribution of REE between clinopyroxene and basaltic melt along a mantle adiabat:  
837 effects of major element composition, water, and temperature. *Contrib. Mineral. Petrol.* **163**, 807–823.  
838 doi:10.1007/s00410-011-0700-x
- 839 Sun S.-s. and McDonough W. F. (1989) Chemical and isotopic systematics of oceanic basalts: implications for mantle  
840 composition and processes. In *Magmatism in the Ocean Basins* (eds. A. D. Saunders and M. J. Norry). Geological  
841 Soc., London, Special Publication. pp. 313–345. doi:10.1144/GSL.SP.1989.042.01.19
- 842 Teng F.-Z., Dauphas N. and Watkins J. M. (eds) (2017) Non-traditional stable isotopes. *Rev. Mineral. Geochem.* **82**.
- 843 Uchimizu M. (1966) Geology and petrology of alkali rocks from Dogo, Oki Islands. *J. Fac. Sci. Univ. Tokyo, Sec. 2* **16**,  
844 85–159.
- 845 Vannucci R., Bottazzi B., Wulff-Pedersen E. and Neumann E.-R. (1998) Partitioning of REE, Y, Sr, Zr and Ti between  
846 clinopyroxene and silicate melts in the mantle under La Palma (Canary Islands): implications for the nature of the  
847 metasomatic agents. *Earth Planet. Sci. Lett.* **158**, 39–51. doi:10.1016/S0012-821X(98)00040-5
- 848 Wang Z., Lazarov M., Steinmann L. K., Becker H., Zou Z. and Geng, X. (2018) The distribution of lead and thallium in  
849 mantle rocks: Insights from the Balmuccia peridotite massif (Italian Alps). *Am. Mineral.* **103**, 1185–1199.  
850 doi:10.2138/am-2018-6423
- 851 Wasylenki L. E., Baker M. B., Kent A. J. R. and Stolper E. M. (2003) Near-solidus melting of the shallow upper  
852 mantle: partial melting experiments on depleted peridotite. *J. Petrol.* **44**, 1163–1191.  
853 doi:10.1093/petrology/44.7.1163
- 854 Weaver B. L. (1991) The origin of ocean island basalt end-member compositions: trace element and isotopic  
855 constraints. *Earth Planet. Sci. Lett.* **104**, 381–397. doi:10.1016/0012-821X(91)90217-6
- 856 Weis D. and Frey F. A. (1991) Isotope geochemistry of Ninetyeast Ridge basement basalts: Sr, Nd, and Pb evidence for  
857 involvement of the Kerguelen hot spot. *Proc. ODP Sci. Results* **121**, 591–610.  
858 doi:10.2973/odp.proc.sr.121.170.1991
- 859 White W. B. (2015) Probing the Earth's deep interior through geochemistry. *Geochem. Perspec.* **4**, 95–251.
- 860 Willbold M. and Stracke A. (2006) Trace element composition of mantle end-members: Implications for recycling of  
861 oceanic and upper and lower continental crust. *Geochem. Geophys. Geosyst.* **7**, Q04004.  
862 doi:10.1029/2005GC001005
- 863 Willbold M. and Stracke A. (2010) Formation of enriched mantle components by recycling of upper and lower  
864 continental crust. *Chem. Geol.* **276**, 188–197. doi:10.1016/j.chemgeo.2010.06.005
- 865 Wood B. J. and Kiseeva E. S. (2015) Trace element partitioning into sulfide: how lithophile elements become  
866 chalcophile and vice versa. *Am. Mineral.* **100** 2371–2379. doi:10.2138/am-2015-5358CCBYNCND

- 867 Wood B. J. and Trigila R. (2001) Experimental determination of aluminous clinopyroxene-melt partition coefficients  
868 for potassic liquids, with application to the evolution of the Roman province potassic magmas. *Chem. Geol.* **172**,  
869 213–223. doi:10.1016/S0009-2541(00)00259-X
- 870 Workman R. K. and Hart S. R. (2005) Major and trace element composition of the depleted MORB mantle (DMM).  
871 *Earth Planet. Sci. Lett.* **231**, 53–72. doi:10.1016/j.epsl.2004.12.005
- 872 Yang S., Humayun M. and Salters V. J. M. (2018) Elemental systematics in MORB glasses from the Mid-Atlantic  
873 Ridge. *Geochem. Geophys. Geosyst.* **19**, 4236–4259. doi:10.1029/2018GC007593
- 874 York D., Evensen N. M., Martínez M. L. and Delgado J. D. B. (2004) Unified equations for the slope, intercept, and  
875 standard errors of the best straight line. *Am. J. Phys.* **72**, 367–375. doi:10.1119/1.1632486
- 876 Zindler A. and Hart S. R. (1986) Chemical geodynamics. *Annu. Rev. Earth Planet. Sci.* **14**, 493–571.
- 877 Zuleger E., Alt J. C. and Erzinger J. (1996) Data report: Trace-element geochemistry of the lower sheeted dike  
878 complex, Hole 504B, Leg 140. *Proc. ODP Sci. Results* **148** 455-466.

879 **Figure captions**

880 **Figure 1:** Plot of  $\epsilon^{205}\text{Tl}$  against Tl concentration. There is no covariation. Large symbols: this study. Other  
881 data sources: [1] Blusztajn et al. (2018); [2] Prytulak et al. (2017); [3] Nielsen et al. (2007); [4] Nielsen et al.  
882 (2006a). \* picrites.

883 **Figure 2:** Primitive Mantle-normalised trace element plots. Note that Tl appears twice (highlighted),  
884 positioned both between Cs and Rb (Prytulak et al., 2017) and between La and Ce (Jenner, 2017). The  
885 ordering otherwise follows that of Willbold and Stracke (2006). For almost all samples there is a clear  
886 negative Tl anomaly regardless of position, as emphasised by the averages for each end-member.

887 **Figure 3:** (a) Ce/Tl and (b) Tl concentrations plotted against MgO contents. Thallium is a highly  
888 incompatible element, and consequently the absolute abundance co-varies with indices of melt  
889 differentiation, such as MgO. However, Ce/Tl ratios do not exhibit co-variation with melt evolution for OIB  
890 samples, indicating that Ce and Tl exhibit similar incompatibility with respect to magmatic processes in the  
891 mantle. Symbols and data sources as in Figure 1.

892 **Figure 4:** Plot of Ce/Tl ratios versus Tl concentrations in oceanic basalts and subduction zone volcanics.  
893 Ce/Tl trends clearly distinguish between tectonic melting regimes for fresh lavas. Note that Hawai 'ian and  
894 Icelandic picritic lavas (dark gray) lie off the general OIB trend to lower Tl concentrations, presumably due  
895 to the larger degree of melting they represent. Large symbols: this study. Other data sources (see Table 2,  
896 Electronic Annex 2): [1] Blusztajn et al. (2018); [2] Prytulak et al. (2017); [3] Nielsen et al. (2007); [4]  
897 Nielsen et al. (2006a); [5] Chauvel et al. (2012); [6] Nielsen et al (2016); [7] Nielsen et al. (2017a); [8]  
898 Prytulak et al. (2013); [9] Prytulak et al. (2017); [10] Shu et al. (2017); [11] Cox et al. (2019); [12] Jenner  
899 and O'Neill (2012); [13] Nielsen et al. (2014); [14] Yang et al. (2018). \* picrites.

900 **Figure 5:** (a) MORB melting model of Nielsen et al. (2014), with  $\text{Tl}_{\text{DM}} = 0.48 \text{ ng/g}$ ,  $\text{S}_{\text{DM}} = 195 \text{ }\mu\text{g/g}$  and  
901  $D_{\text{sulf/sil}}^{\text{Tl}} = 36$  (for other parameters see Table 5). (b) Modified MORB melting model assuming  $\text{S}_{\text{DM}} = 100$   
902  $\mu\text{g/g}$  and  $D_{\text{sulf/sil}}^{\text{Tl}} = 10$ ; lower  $D_{\text{sulf/sil}}^{\text{Tl}}$  increases the melt percentage required to achieve any given Tl-Ce/Tl  
903 data pair. In this modified model we permit variation of  $D_{\text{cpx/melt}}^{\text{Ce}}$  (see text, Table 5), reproducing both the  
904 average MORB Ce/Tl and the sense of variation. Best fit is achieved with a lower  $\text{Tl}_{\text{DM}}$  of  $0.27 \text{ ng/g}$ ,  
905 implying a DM Ce/Tl of  $\sim 1800$ . (c) Modified model with variable Tl (see legend),  $\text{Ce} = 0.55 \text{ }\mu\text{g/g}$ ,  $\text{S} = 100$

906  $\mu\text{g/g}$ ,  $D^{\text{Tl}}_{\text{sulf/sil}} = 10$ ,  $D^{\text{Ce}}_{\text{cpx/melt}} = 0.1$  (d) Modified melting model with  $\text{Tl} = 0.27 \text{ ng/g}$ , variable Ce (see legend;  
907 Workman and Hart, 2005), and other values as for subfigure (c). Symbols and data sources as in Figure 4.

908 **Figure 6:** (a) Melting of PM (grey) and DM (black) sources (Table 6) with varying  $D^{\text{Ce}}_{\text{cpx/melt}}$ . (b) Melting of  
909 (i) a hypothetical mixed source with  $\text{Tl} = 1 \text{ ng/g}$ ,  $\text{Ce} = 15 \mu\text{g/g}$ , and  $D^{\text{Ce}}_{\text{cpx/melt}} = 0.8$ ; and (ii) a hypothetical  
910 mixed source with  $\text{Tl} = 0.5 \text{ ng/g}$ ,  $\text{Ce} = 5 \mu\text{g/g}$ , and  $D^{\text{Ce}}_{\text{cpx/melt}} = 0.15$ . (c) 3-5% melting of a hypothetical  
911 source with  $\text{Ce} = 5 \mu\text{g/g}$  and  $D^{\text{Ce}}_{\text{cpx/melt}} = 0.1$ . Source Tl concentration varies as indicated on figure. (d) As  
912 subfigure (c), but instead  $\text{Ce} = 15 \mu\text{g/g}$  and  $D^{\text{Ce}}_{\text{cpx/melt}} = 0.5$ . Symbols and data sources as in Figure 4. All  
913 displayed models assume  $100 \mu\text{g/g}$  S (Ding and Dasgupta, 2018) and  $D^{\text{Tl}}_{\text{sulf/sil}} = 10$ . All melting percentages  
914 as marked on subfigure (a).

915 **Figure 7:** Plots of  $\epsilon^{205}\text{Tl}$  against (a)  $^{87}\text{Sr}/^{86}\text{Sr}$ , (b)  $^{143}\text{Nd}/^{144}\text{Nd}$ , (c)  $^{176}\text{Hf}/^{177}\text{Hf}$ , (d)  $^{206}\text{Pb}/^{204}\text{Pb}$ , (e)  $^{207}\text{Pb}/^{204}\text{Pb}$ ,  
916 (f)  $^{208}\text{Pb}/^{204}\text{Pb}$ . For OIB samples, there is no co-variation of  $\epsilon^{205}\text{Tl}$  and the radiogenic isotope systems  
917 commonly used to define mantle components, with the possible exception of  $^{143}\text{Nd}/^{144}\text{Nd}$  in Icelandic  
918 picrites. Error bars are generally smaller than symbols. Symbols and data sources as in Figure 4.

919 **Figure 8:** Plots of ratios employed to track AOC contributions to OIB source against  $\epsilon^{205}\text{Tl}$ . (a) Ce/Tl against  
920  $\epsilon^{205}\text{Tl}$ , showing literature main-phase St Helena lavas and St Helena samples from this study, (b) Ce/Tl  
921 against  $\epsilon^{205}\text{Tl}$  for all OIB samples, (c) Ce/Pb against  $\epsilon^{205}\text{Tl}$  with the same samples as subfigure (a), (d) Ce/Pb  
922 against  $\epsilon^{205}\text{Tl}$  for all OIB samples. Blusztajn et al. (2018) argued that a sense of correlation for main-phase St  
923 Helena lavas indicated a role for subduction-processed AOC in generating the HIMU array. However, this  
924 trend is not replicated in HIMU lavas from other localities, and is not unique to HIMU-type lavas. Symbols  
925 and data sources as in Figure 4.

926 **Figure 9:** Plot of  $\epsilon^{205}\text{Tl}$  against  $\text{Tl}/\text{Tl}^*$  ratios.  $\text{Tl}^* = \text{Brett\_etal\_GCA\_Eqn1.pdf}$  or

927 **Brett\\_etal\\_GCA\\_Eqn2.pdf**, where N denotes concentration values normalised to PM (a,c), or DM (b,d).

928 Relative to Cs and Rb,  $\text{Tl}/\text{Tl}^*$  values  $> 0.5$  (for both PM and DM normalisations) are associated with Tl  
929 isotopic compositions that are distinct from the mantle range (green band). Relative to La and Ce, it is less  
930 clear whether there is any association. Symbols and data sources as in Figure 4.

931 **Figure A1:**  $D^{\text{Ce}}_{\text{cpx/melt}}$  values versus CaO in clinopyroxene. This illustrative plot has not been corrected for  
932 pressure and temperature, or for other compositional variables including degree of hydration. With the  
933 notable exception of Green et al. (2000) and the two McDade studies, which examine melting under strongly

934 hydrous conditions, there is a general sense of increasing Ce compatibility as CaO in cpx increases both  
935 within and between studies.

937 **Table 1.** Summary of OIB localities with published Tl concentration and isotopic composition data.

Locality	FOZO/PREMA		EMI		EM		HIMU		
	Hawai'i	Iceland	Gough	Tristan	Marquesas <sup>†</sup>	Azores	St Helena	Rurutu	Tubuai
literature [Tl]	x	x			x	x	x		
literature $\epsilon^{205}\text{Tl}$	x	x				x	x		
$^{87}\text{Sr}/^{86}\text{Sr}$	o	range	x	x	x	x	x	x	x
$^{143}\text{Nd}/^{144}\text{Nd}$	o	x	x	x	x	x	x	x	x
$^{176}\text{Hf}/^{177}\text{Hf}$		range	x	x	x		x		o
Pb isotopes	x	range			x	x	x	x	x
this study			x	x	x		x	x	x
key references	1*	2*,3	4,5	4,5	6	2	4,5,7	8	9

938

939 \* picrites.

940 † Note that Marquesas lavas exhibit variable composition covering a very wide range of radiogenic isotopic  
941 compositions.

942 x = data exists; o = partial data; range = a range is known, but samples have not been individually analysed.

943 [1] Nielsen et al. (2006a); [2] Nielsen et al. (2007); [3] Prytulak et al. (2017); [4] Willbold and Stracke

944 (2006); [5] Willbold and Stracke (2010); [6] Chauvel et al. (2012); [7] Blusztajn et al. (2018); [8] Chauvel et

945 al. (1997); [9] Chauvel et al. (1992).

**Table 2.** Key geochemical data for OIB samples analysed in this study.

Sample	MgO* (wt%)	Ce ( $\mu\text{g/g}$ )	Tl (ng/g)	Ce/Tl	$\epsilon^{205}\text{Tl}$	2sd	Dissolutions	Measurements (n)
<i>Gough (EMI)</i>								
G6	7.94	101	26	3915	0.5	2.2	2	3 (1 NU + 2 NUII)
G102	5.28	107	76	1402	-2.5	0.6	2	3
G117	4.52	113	39	2921	3.8	0.6	1	4
G118	12.97	73.9	49	1495	-0.6	0.5	1	2
G132	5.04	87.1	95	919	-4.6	0.5	1	3
G135	5.85	112	53	2104	-0.6	0.5	1	2
B167	3.39	107	74	1437	-3.2	0.5	1	1
<i>Tristan da Cunha (EMI)</i>								
T16	4.74	134	101	1321	-2.3	0.5	1	2
T60	12.2	60.9	38	1600	-0.3	0.5	1	2
T64	8.91	115	64	1796	-1.1	0.5	1	1
T122	7.28	104	55	1888	-1.2	0.5	1	2
T497	7.61	136	87	1559	-1.2	0.8	2	9
T557	8	112	56	2006	-1.2	1.5	2	7
<i>T557 (leached)</i>					-1.6	0.9	1	1 (NUII)
<i>Fatu Hiva, Marquesas (EM<sup>†</sup>)</i>								
FH01	10.6	110	7	16740	0.0	1.3	1	1
FH11	6.8	99.0	26	3837	-3.6	0.8	2	3
FH18	12.2	81.5	32	2554	-1.8	0.5	1	1
<i>Hiva Oa, Marquesas (EM<sup>†</sup>)</i>								
HV64	8	81.1	17	4649	0.7	0.5	1	1
HV76	5.14	72.7	63	1162	-0.3	0.7	1	2
<i>Montane, Marquesas (EM<sup>†</sup>)</i>								
MT04	5.63	71.6	18	3996	-3.9	1.0	3	3 (2 NU + 1 NUII)
MT08	5.53	82.0	25	3224	0.6	0.5	2	2
<i>Tahuata, Marquesas (EM<sup>†</sup>)</i>								
TH4	6.37	108	77	1415	-2.9	0.5	1	1
TH5	7.44	137	66	2064	-0.5	0.5	1	2
TH8	4.67	96.3	24	4045	1.0	0.5	1	1
<i>TH8 (leached)</i>					2.2	0.9	1	1 (NUII)
TH13	6.09	80.7	15	5482	-3.5	0.6	2	4
TH14	8.37	109	177	614	-6.4	0.5	1	4
TH18	6.4	87.6	43	2014	0.4	1.2	2	3 (2 NU + 1 NUII)
<i>TH18 (leached)</i>					-0.2	0.8	1	1 (Nu II)
TH31	5.6	82.1	18	4574	-1.9	1.1	2	2 (1 NU + 1 NUII)
TH39	9.2	81.5	18	4533	4.4	0.9	1	1
<i>Ua Huka, Marquesas (EM<sup>†</sup>)</i>								
UH53	0.38	155	235	663	-1.8	0.5	1	4
UH81	7.75	90.4	121	748	-1.9	0.5	2	5
UH89	7.2	89.8	39	2278	-3.5	0.5	1	3
UH93	9.85	72.8	97	753	-1.2	0.5	2	3
<i>St Helena (HIMU)</i>								

H28	6.64	101	26	3936	-0.9	0.5	1	5
H38	15.87	41.3	40	1043	-3.1	0.5	1	2
H64	10.97	61.7	14	4360	-0.7	0.5	1	2
H69	9.09	62.8	94	665	-3.3	0.9	2	9
<b>Rurutu, Austral-Cook (HIMU)</b>								
RRT032	6.02	47.9	45	1073	-6.4	1.3	2	4
RRT037	7.4	59.8	40	1489	6.6	0.5	1	1
<i>RRT037 (leached)</i>					4.9	0.9	1	1 (NUII)
74-386	7.24	56.5	14	4024	-2.3	0.5	2	2
74-390	6.29	74.9	44	1709	-6.3	0.5	1	1
<i>74-390 (leached)</i>					-3.7	0.9	1	1 (NUII)
74-396	7.89	73.9	32	2290	-3.4	0.5	1	3
<b>Tubuai, Austral-Cook (HIMU)</b>								
TBA9	17.9	96.4	18	5371	-2.1	1.2	1	2 (NUII)
K109	15.5	117	19	6108	-5.9	0.5	1	1
108B	10.85	88.4	10	9069	-3.1	0.5	1	2
5433	6.2	145	31	4691	-0.3	0.5	1	2
5434	11.26	84.0	25	3393	-3.5	0.5	1	2
5435	4.85	226	50	4497	-4.8	2.4	2	3 (1 NU + 2 NUII)
5436	9.59	111	12	9279	-2.1	0.5	1	1

948

949 \* MgO values per Table 1 and references therein (see Electronic Annex 2b for full details)

950 † Marquesas lavas exhibit variable composition: at a given  $^{87}\text{Sr}/^{86}\text{Sr}$  value, lavas from the 'Ua Huka' group  
951 (Ua Huka, young Hiva Oa) have higher Nd isotopic compositions, and lavas from the 'Fatu Hiva' group  
952 (Fatu Hiva, old Hiva Oa, Montane, Tahuata) have higher  $^{206}\text{Pb}/^{204}\text{Pb}$  (see Chauvel et al., 2012; Electronic  
953 Annex 2).

954 2sd is quoted as the highest of (1) the uncertainty for repeat analyses of BCR-2 on the *Nu HR*, (2) the  
955 uncertainty for repeated measurements of the Aldrich Tl solution on the *Nu Plasma II*, or (3) the uncertainty  
956 for repeat analyses of a given sample.

957 **Table 3.** Slopes obtained for York regressions (York et al., 2004) between log[Tl] and log[Element] (see  
958 text). For MORB, n = 909 except Cs, for which n = 702. For OIB, n = 48.  
959

<b>Element</b>	<b>MORB</b>		<b>OIB</b>	
	slope	2sd	slope	2sd
Ce	0.994	0.030	0.102	0.122
Cs	2.608		2.033	0.571
La	1.285	0.047	0.116	0.136
Pb	0.875	0.021	1.131	0.488
Rb	3.114	0.218	1.091	0.504

960

961 **Table 4.** Modal mineralogy and reaction coefficients used in melting models.

962

<b>mineral</b>	<i>spinel lherzolite (MORB)</i>		<i>garnet lherzolite (OIB)</i>	
	<b>vol proportion (%)<sup>1</sup></b>	<b>melting coefficient<sup>2</sup></b>	<b>vol proportion (%)<sup>3</sup></b>	<b>melting coefficient<sup>3</sup></b>
olivine	0.57	-0.2	0.55	0.08
clinopyroxene	0.13	0.8	0.25	0.81
orthopyroxene	0.28	0.32	0.15	-0.19
spinel	0.02	0.08	-	-
garnet	-	-	0.05	0.3
sulphide	variable	SCSS*	variable	SCSS

963

964 \* Sulphur concentration at sulphide saturation for basaltic melts (Liu et al., 2007; Mavrogenes and O'Neill,  
965 1999; O'Neill and Mavrogenes, 2002). [1] Workman and Hart (2005); [2] Baker and Stolper (1994) and  
966 Wasylenki et al. (2003), as modified by Nielsen et al. (2014); [3] Elliott et al. (2007).

967 **Table 5.** Parameters used in models of MORB and OIB melting.  
 968

Variable	Symbol	<i>Nielsen et al. 2014 (MORB)</i>		<i>MORB</i>		<i>OIB</i>	
		Value range	References	Value range	References	Value range	References
<i>Melting</i>							
melt fraction	F	0-16%	-	0-16%	-	0-18%	-
melt increment		0.01%	-	0.1%	-	0.1%	-
pressure (avg)		1.5 GPa	-	1.5 GPa	-	3 GPa	-
temperature (avg)		1350 °C	-	1350 °C	-	1445 °C	-
FeO in melt		~10%	8	~10%	8	~10%	<i>sample data</i>
SCSS		1200 µg/g	9-11	1200 µg/g	9-11	1200 µg/g	9-11
<i>Partition coefficients</i>							
Thallium	D <sub>cpx/melt</sub>	0.0006	1	0.0006	1	0.0006	1
	D <sub>opx/melt</sub>	0.00045	1	0.00045	1	0.00045	1
	D <sub>ol/melt</sub>	4.5 x 10 <sup>-5</sup>	1	4.5 x 10 <sup>-5</sup>	1	4.5 x 10 <sup>-5</sup>	1
	D <sub>sp/melt</sub>	0	1	0	1	-	-
	D <sub>gt/melt</sub>	-	-	-	-	0	<i>assumed (3)</i>
	D <sub>sulf/melt</sub>	18-100	<i>model</i>	1-25	<i>model</i>	1-25	<i>model</i>
	Bulk D	0.0002-0.11		0.0002-0.028		0.0002-0.007	
Cerium	D <sub>cpx/melt</sub>	0.14	2	0.01-0.8	4-7	0.01-0.8	4-7
	D <sub>opx/melt</sub>	0.006	2	0.006	2	0.0026	7
	D <sub>ol/melt</sub>	4 x 10 <sup>-5</sup>	2	4 x 10 <sup>-5</sup>	2	4 x 10 <sup>-5</sup>	2
	D <sub>sp/melt</sub>	0	<i>assumed</i>	0	<i>assumed</i>	-	-
	D <sub>gt/melt</sub>	-	-	-	-	0.003	3
	D <sub>sulf/melt</sub>	0	<i>assumed</i>	0	<i>assumed</i>	0	<i>assumed</i>
	Bulk D	0.02		0.003-0.1		0.002-0.16	

969 [1] Assumed identical to Rb partition coefficients of Donnelly et al. (2004); [2] McDade et al. (2003a); [3]  
 970 Adam and Green (2006) were unable to determine a partition coefficient for Tl between garnet and silicate  
 971 melt, but for LILE values were very low; [4] Frey (1969); [5] Irving and Frey (1984); [6] Nagasawa et al.  
 972 (1969); [7] Matsui et al. (1977); [8] Gale et al. (2013); [9] Liu et al. (2007); [10] Mavrogenes and O'Neill  
 973 (1999); [11] O'Neill and Mavrogenes (2002).  
 974

975 **Table 6.** Estimated Ce, S and Tl concentrations in potential contributions to OIB source regions.  
 976

<b>Reservoirs</b>	<b>Ce (<math>\mu\text{g/g}</math>)</b>	<b>References</b>	<b>Tl (<math>\text{ng/g}</math>)</b>	<b>References</b>	<b>S (<math>\mu\text{g/g}</math>)*</b>	<b>References</b>
DM	0.55	1	0.27-0.48	9; <i>model</i>	0-400	2; <i>model</i>
PM	1.675	2	3.5	2	0-400	2; <i>model</i>
Peridotites	0.020-0.39	3	0.05-3.5	3	76-360	3,12
FeMn sediment (hydrogenetic)	700	8	90000	11	-	-
Subducted eclogites†	20 (1-210)	13	60 (2-350)	13	-	-
Subduction-processed oceanic crust	~10-75	<i>calculated</i>	~2-6	<i>calculated</i>	-	-

977  
 978 \* Sulphide abundance was converted to S concentration using the assumption that on average mantle  
 979 sulphides are 36 wt% S, i.e. dominantly FeNi sulphides. † mean (range). [1] Workman and Hart (2005); [2]  
 980 McDonough and Sun (1995); [3] Wang et al. (2018); [4] Sparks (1995); [5] Zuleger et al. (1996); [6] Bach et  
 981 al. (1996); [7] Sun and McDonough (1989); [8] Piper (1974); [9] Nielsen et al. (2014); [10] Nielsen et al.  
 982 (2006b); [11] Rehkämper et al. (2002); [12] Ding and Dasgupta (2018); [13] Shu et al. (2019).

983 **Supplementary Figures**

984 **Figure S1:** Plot of  $\epsilon^{205}\text{Tl}$  against MgO content for samples of this study and from the literature.  $\epsilon^{205}\text{Tl}$  does  
 985 not vary systematically with melt evolution. As the majority of samples are not cogenetic, two suites of lavas  
 986 following common liquid lines of descent (Hekla, Iceland; Anatahan, Marianas) are highlighted, showing  
 987 that even at low MgO there is no correlation with  $\epsilon^{205}\text{Tl}$ . Approximate fields of fractionating phases are  
 988 indicated. Data sources: [1] Prytulak et al. (2017); [2] Blusztajn et al. (2018); [3] Nielsen et al. (2007); [4]  
 989 Nielsen et al. (2006a). \* picrites.

990 **Figure S2:** Depleted Mantle-normalised trace element plots. Here the negative Tl anomaly, while still  
 991 present on average, is less pronounced – particularly for EM-type lavas.

992 **Figure S3:** Tl anomaly exhibits clearer covariation with absolute Tl abundance when calculated relative to  
 993 REE than when calculated relative to LILE (with the possible exception of HIMU). Symbols and data  
 994 sources as in Figure 5.

995 **Figure S4:** Plot of La/Tl, Pb/Tl, Rb/Tl and Cs/Tl ratios against Tl concentration. Only the La/Tl ratios  
 996 distinguishes tectonic settings as clearly as the Ce/Tl ratios. Symbols and data sources as in Figure 5.

997 **Figure S5:** Process identification plot (Minster and Allègre, 1978) of Tl/Ce against 1/Tl. Also shown are  
 998 melting patterns (melt fraction  $F = 0.0001$  to 1) for DM (Tl = 0.00038  $\mu\text{g/g}$ , Ce = 0.772  $\mu\text{g/g}$ ) and PM (Tl =  
 999 0.0035  $\mu\text{g/g}$ , Ce = 1.675  $\mu\text{g/g}$ ), in addition to the fractional crystallisation trend ( $F = 1$  to 0.1), assuming bulk  
 1000  $D_{\text{Tl}} = 0.02$  and bulk  $D_{\text{Ce}} = 0.06$ . While most of the variation in OIB is subparallel to the DM melting trend,  
 1001 with scatter leaving room for some fractional crystallisation, the observed range significantly exceeds that  
 1002 which can be explained simply through a combination of melting and fractional crystallisation. The OIB  
 1003 trend therefore requires mixing melts from different sources, one of which cannot contain more than  
 1004 negligible Tl (note y-intercept of trend). Symbols and data sources as in Figure 5.

1005 **Figure S6:** Mixing between St Helena HIMU average composition (Blusztajn et al., 2018) and three “AOC”  
 1006 values (see Table S1). Ticks correspond to admixture of 10%, 20% and 30% of AOC as labelled for ODP  
 1007 504B.

	DM	St Helena average	ODP 504B (~6.6 Ma)	DSDP 417/418 (~109 Ma)	“Modern AOC”
Tl ( $\mu\text{g/g}$ )	0.00038	0.03	0.25	0.07	<u>0.017</u>
Ce ( $\mu\text{g/g}$ )	0.772	80.83	4.31	6.19	<u>12</u>
Pb ( $\mu\text{g/g}$ )	0.0232	2.06	0.36	0.69	<u>0.6</u>
Ce/Pb	33	~40	12	9	20
$\epsilon^{205}\text{Tl}$	-2	~-2	-15	-5.4	-15

1008

1009 **Table S1.** For DM, values are taken from Salters and Stracke (2004), except  $\epsilon^{205}\text{Tl}$  (Nielsen et al., 2006a).  
 1010 For DSDP 417/418, supercomposite values are taken from Blusztajn et al. (2018) and Staudigel et al. (1995).  
 1011 ODP 504B values are taken from Nielsen et al. (2006b) and Bach et al. (2003). “Modern AOC” values are

1012 taken from Blusztajn et al. (2018) or inferred (underlined). St Helena average values are as reported by  
1035

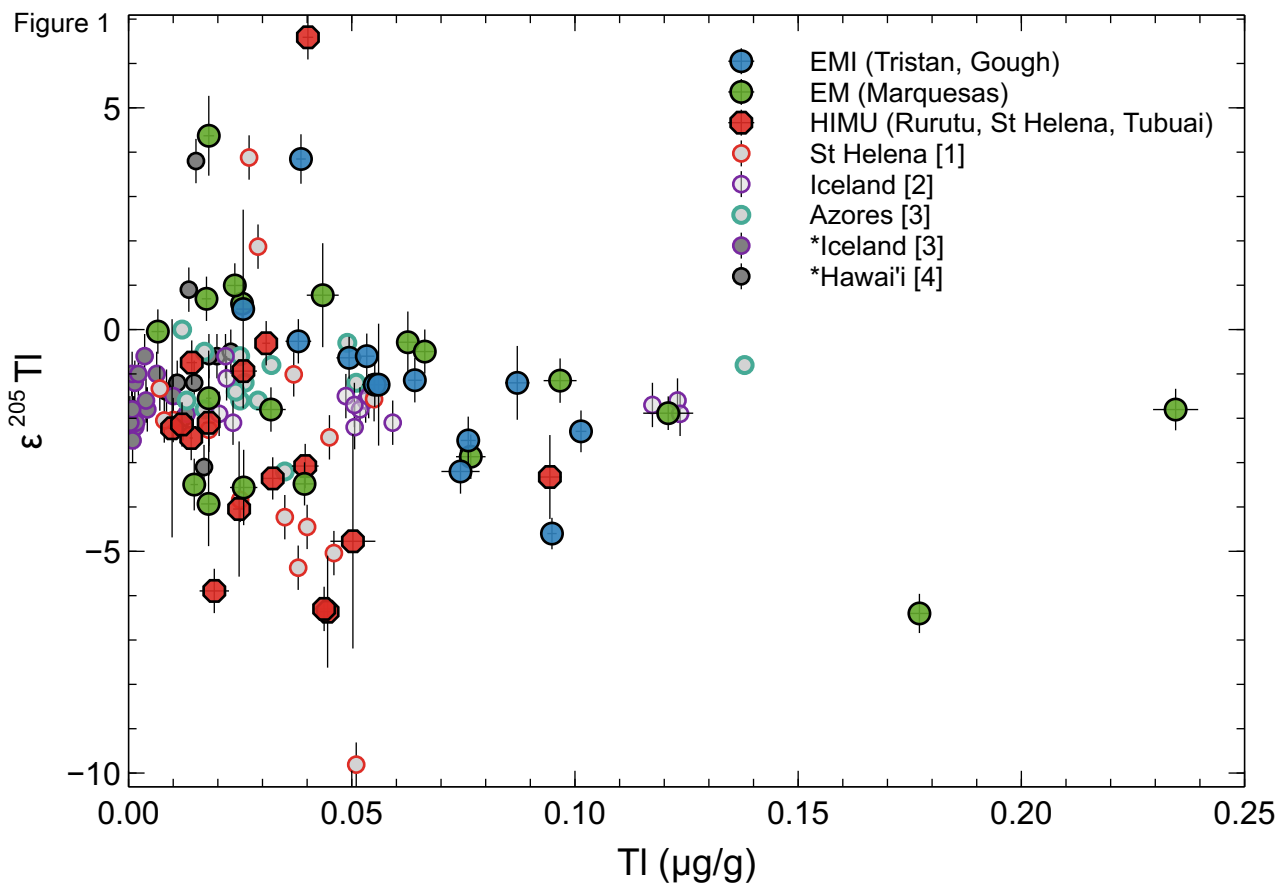


Figure 2

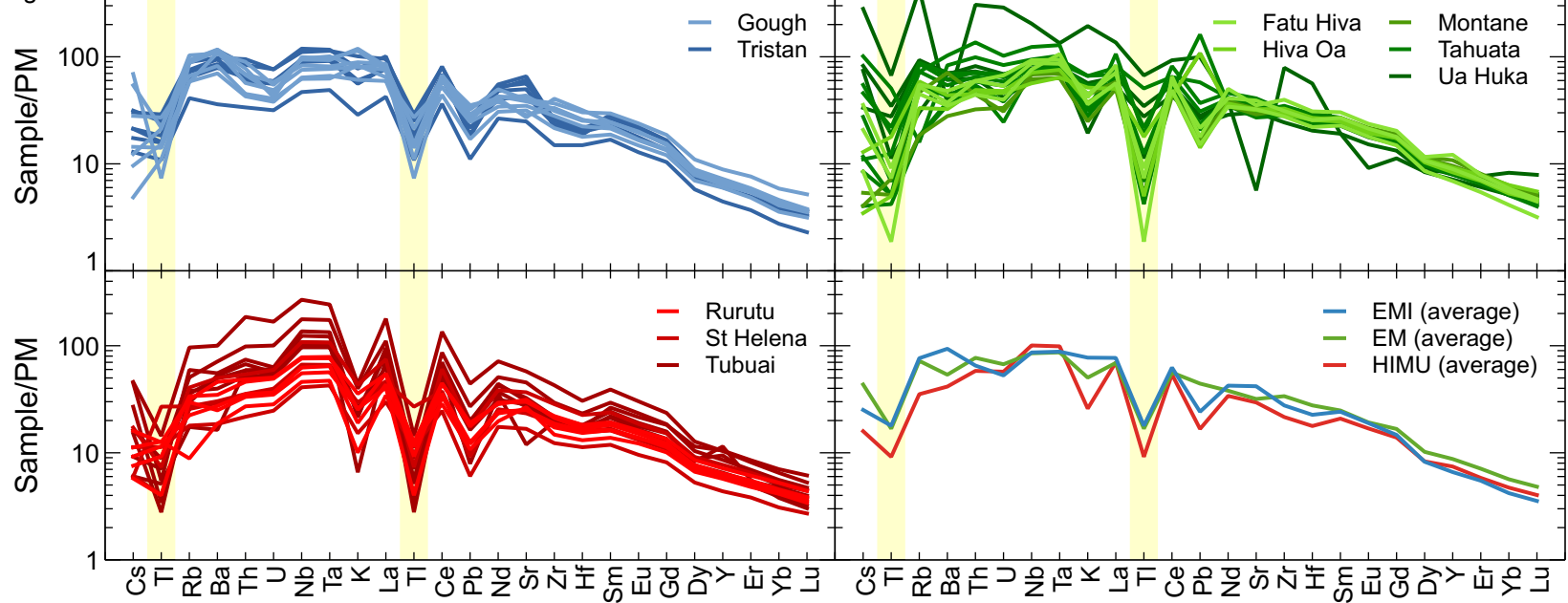
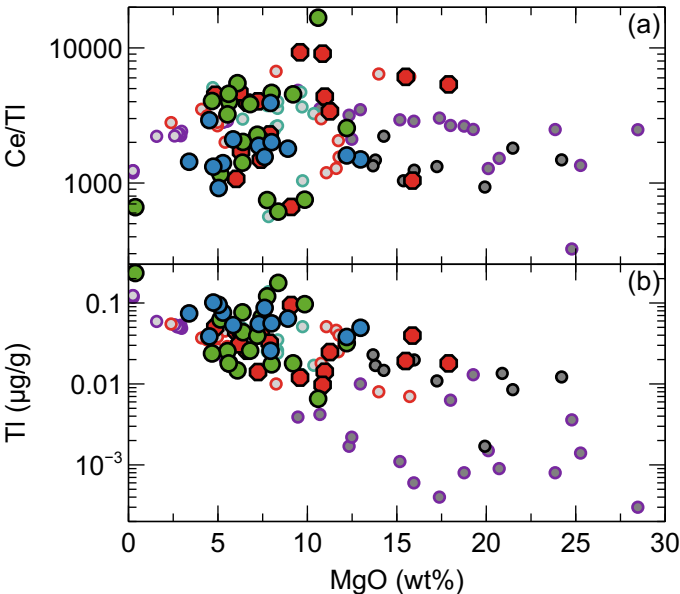


Figure 3

- EMI (Gough, Tristan)
- EM (Marquesas)
- HIMU (St Helena, Rurutu, Tubuai)
- St Helena [1]
- Iceland [2]
- Azores [3]
- \*Iceland [3]
- \*Hawai'i [4]



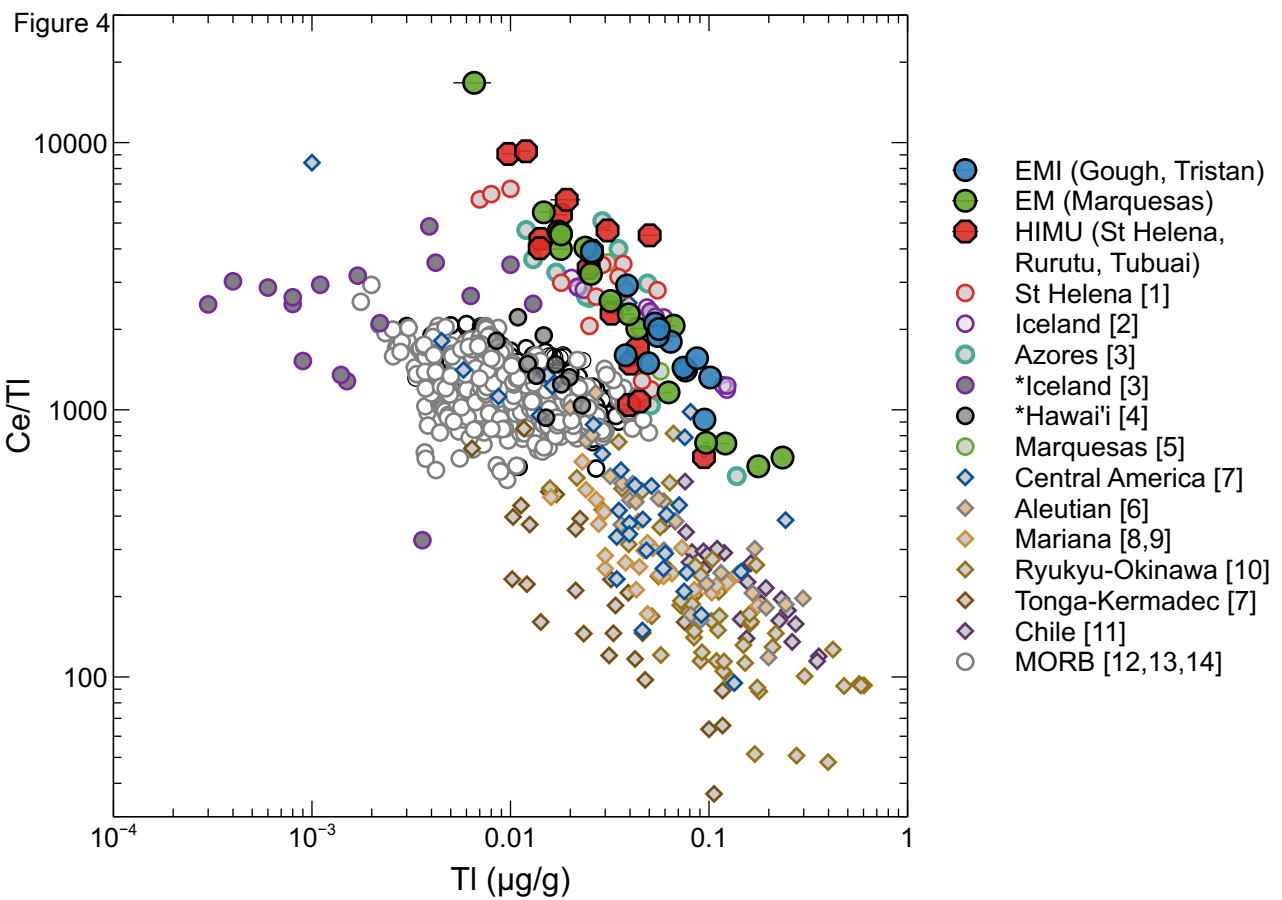
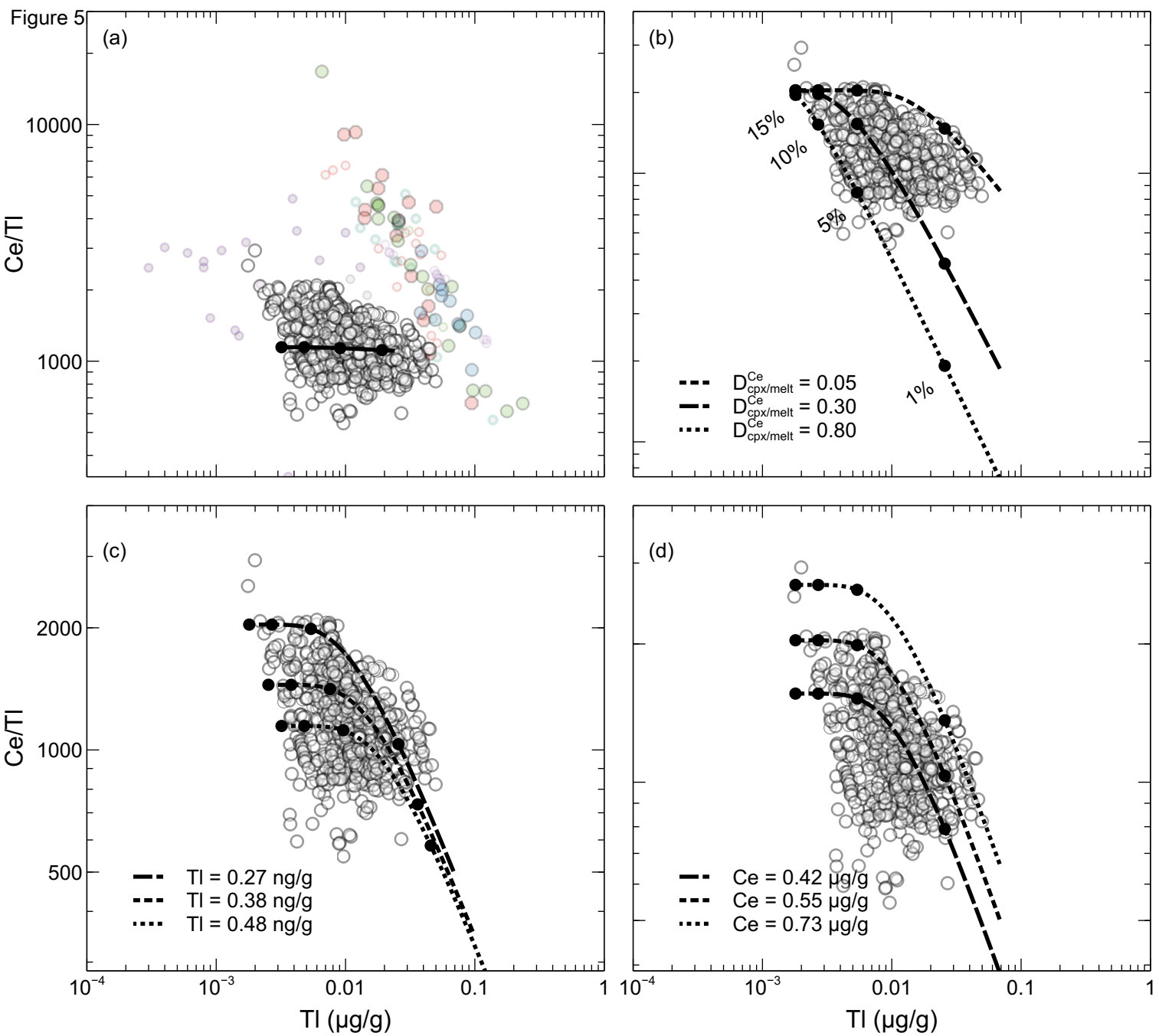
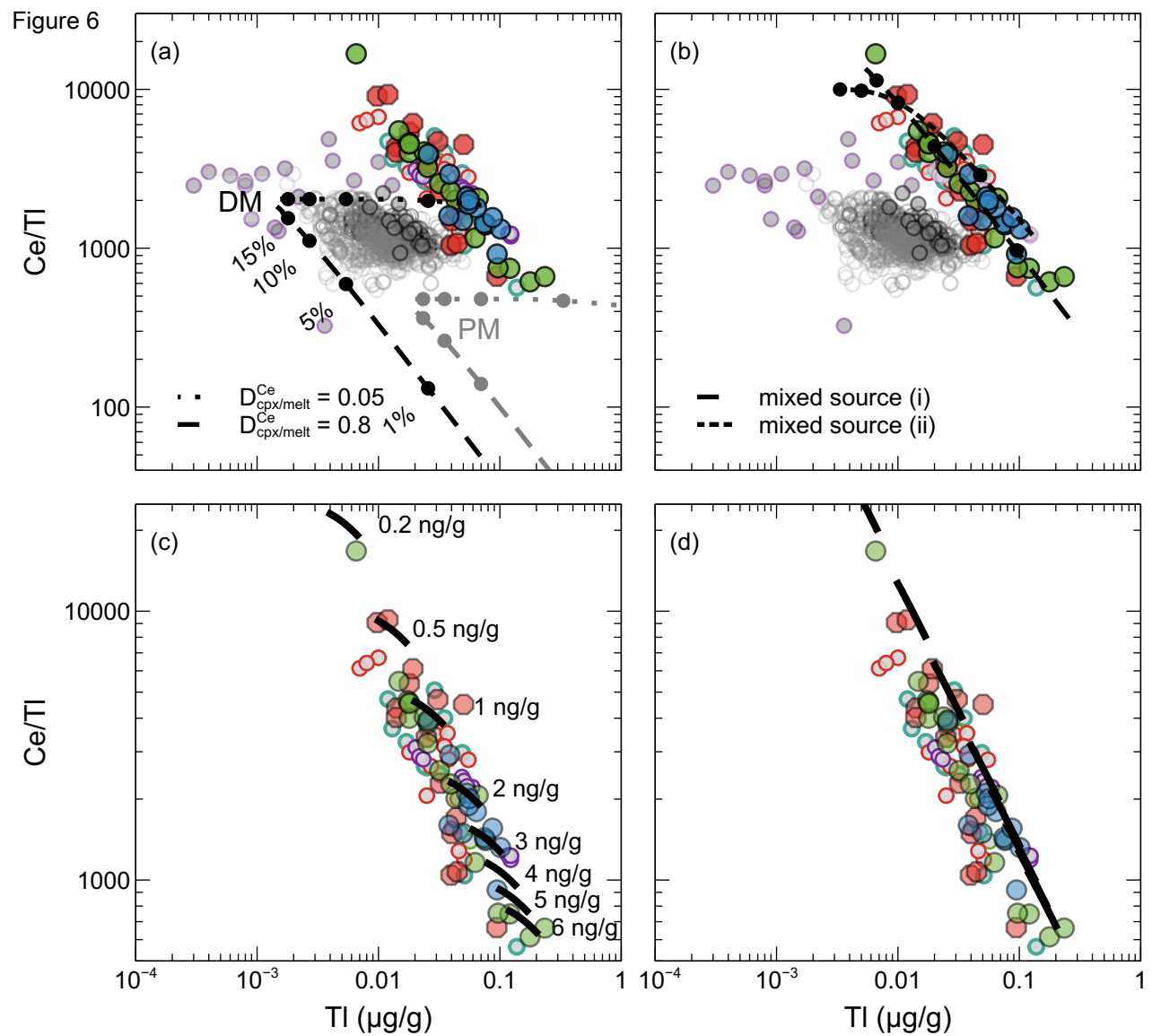


Figure 5





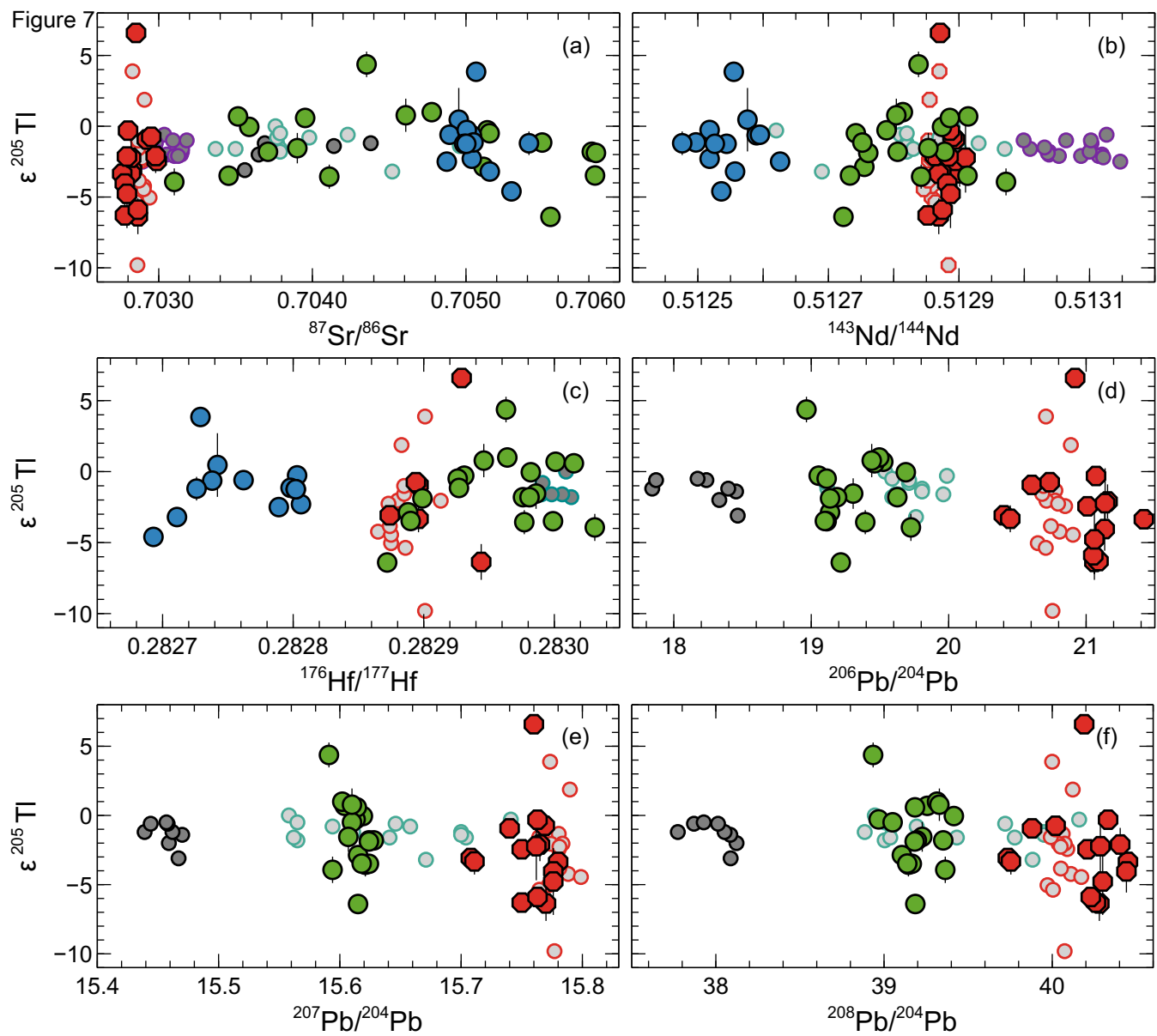


Figure 8

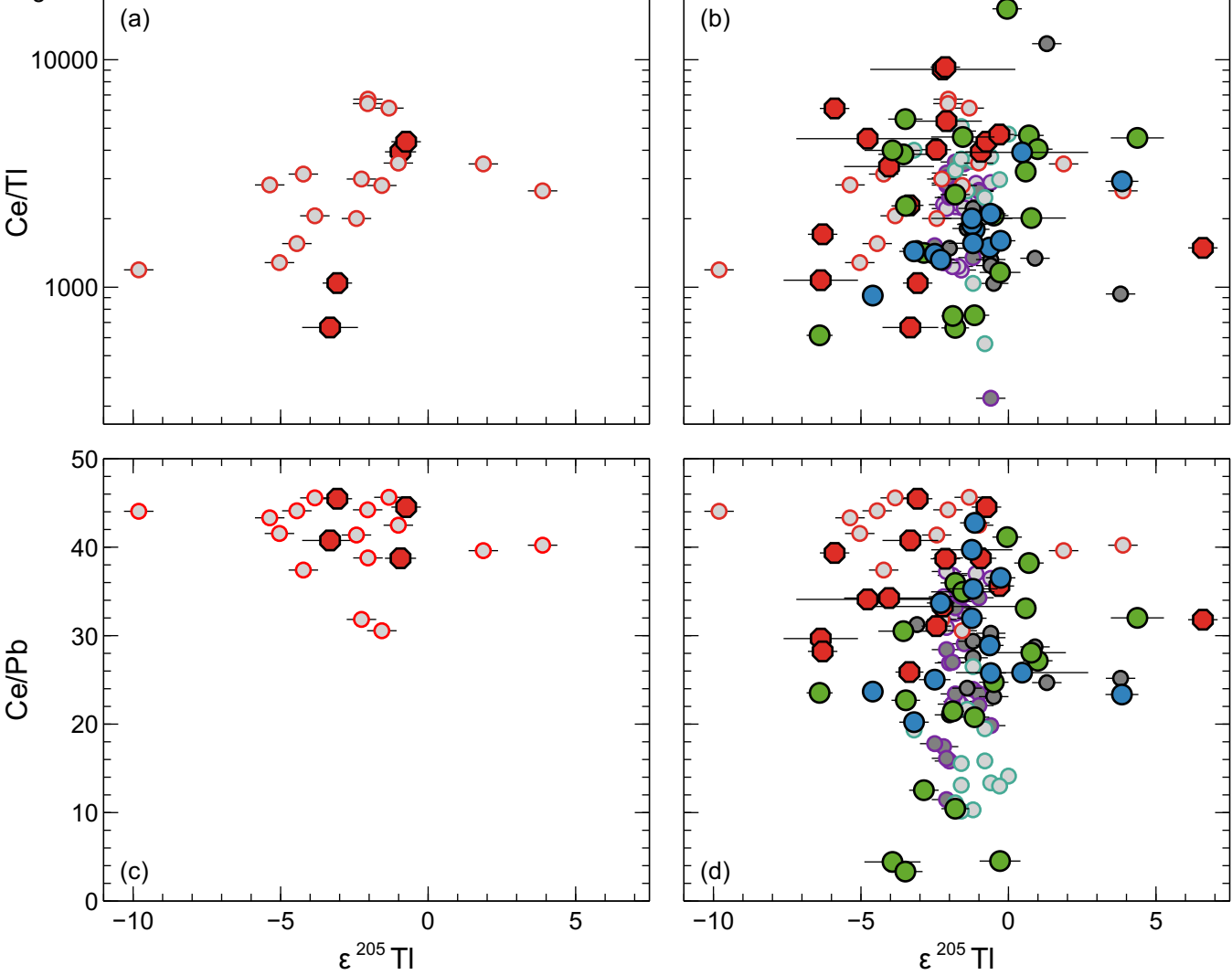
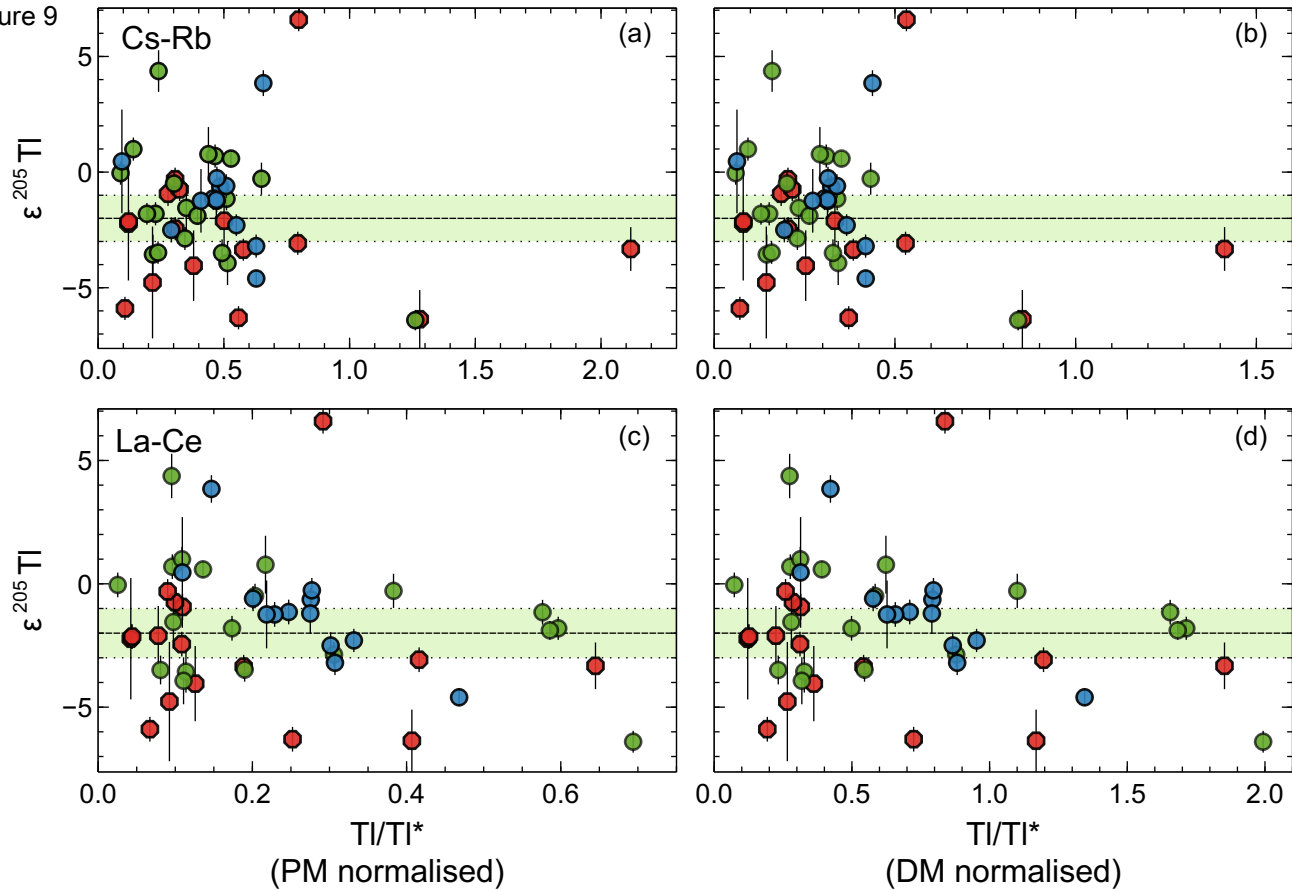


Figure 9



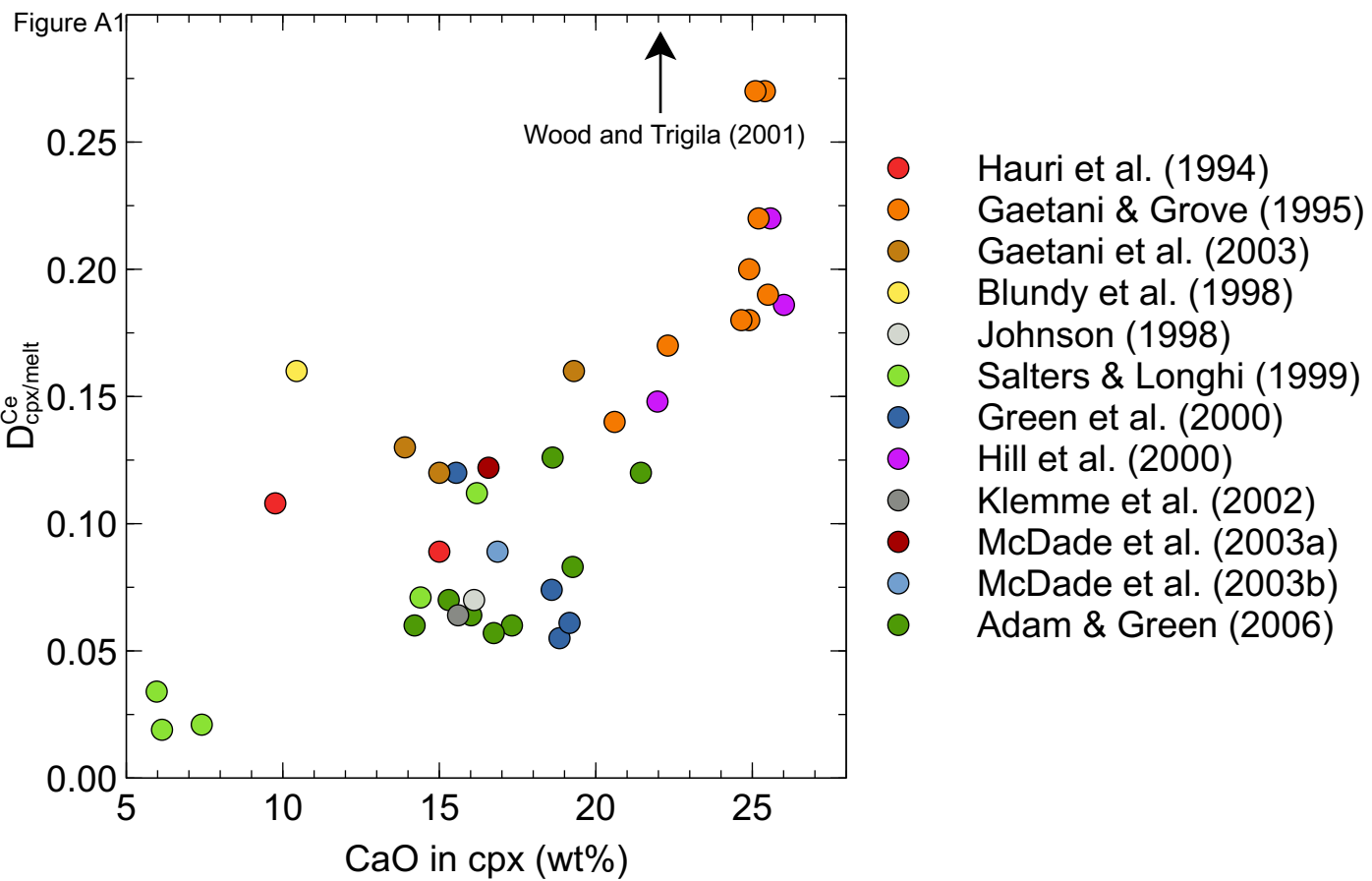
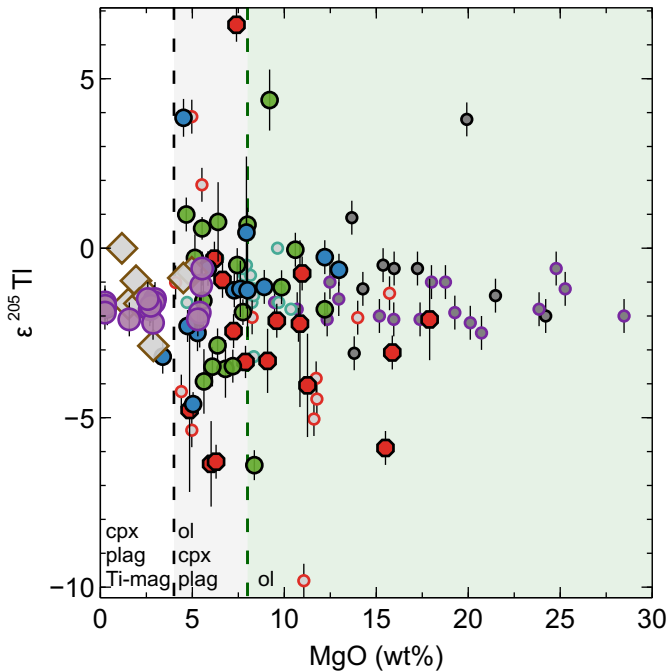
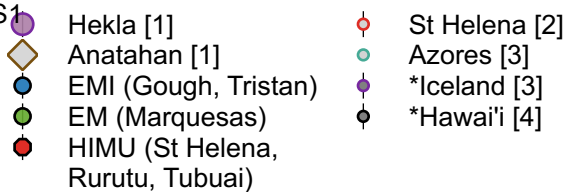
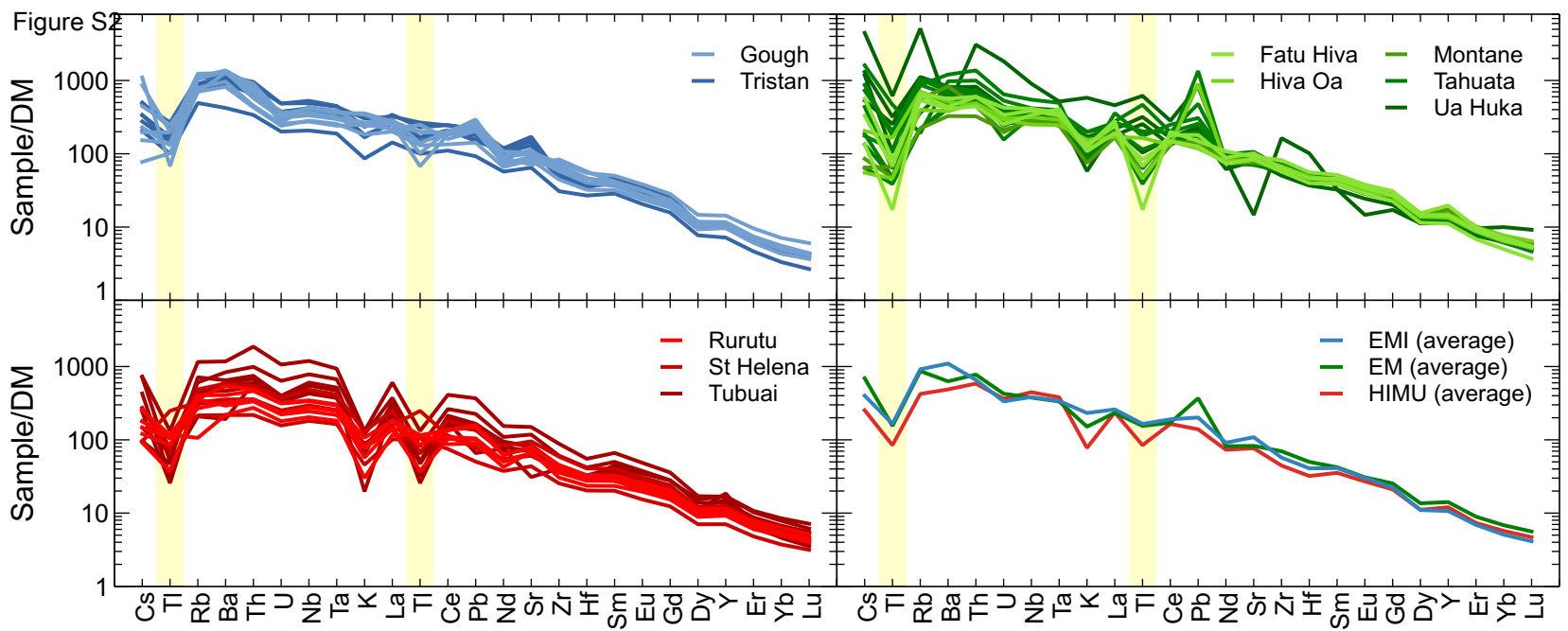
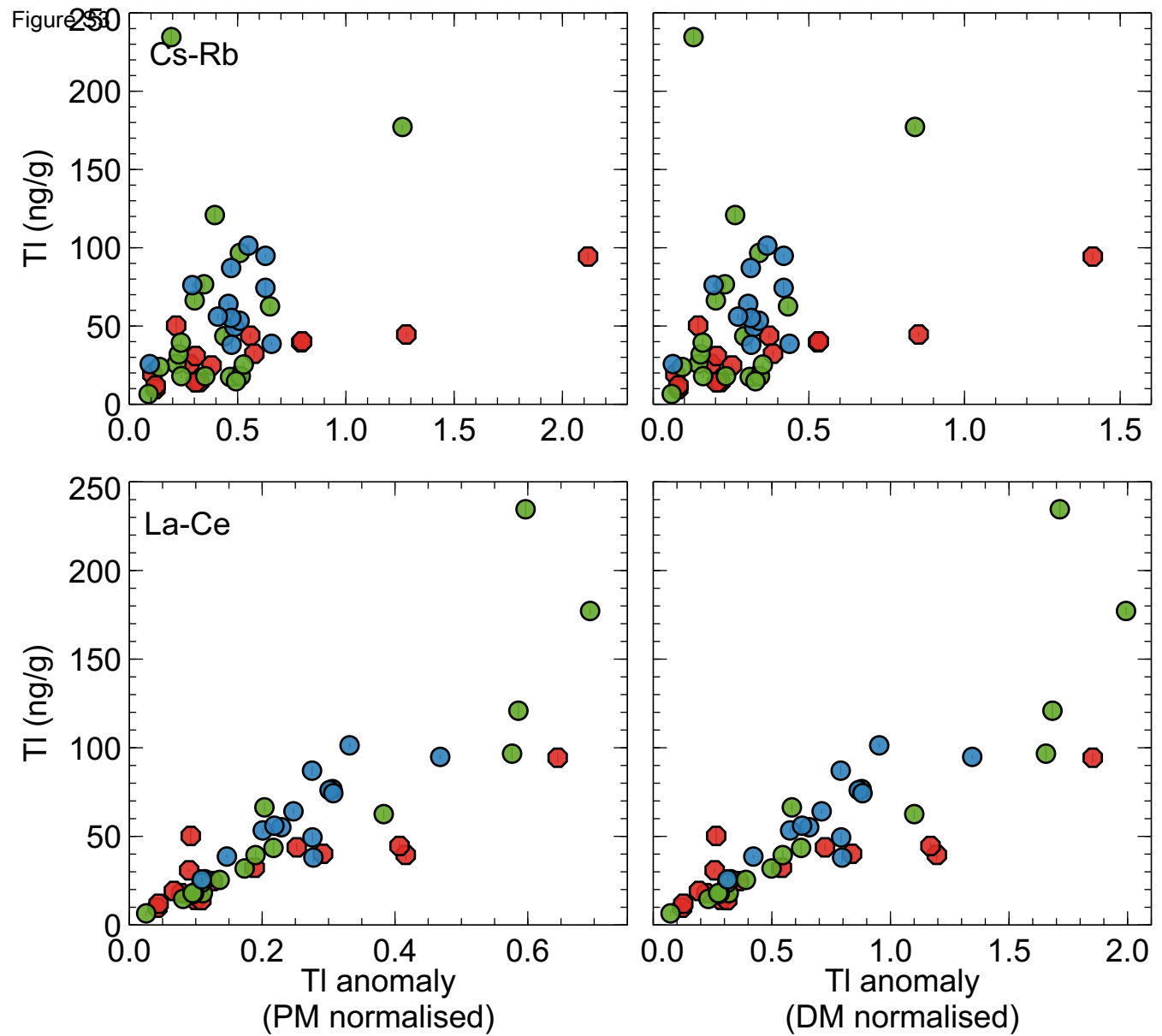


Figure S1







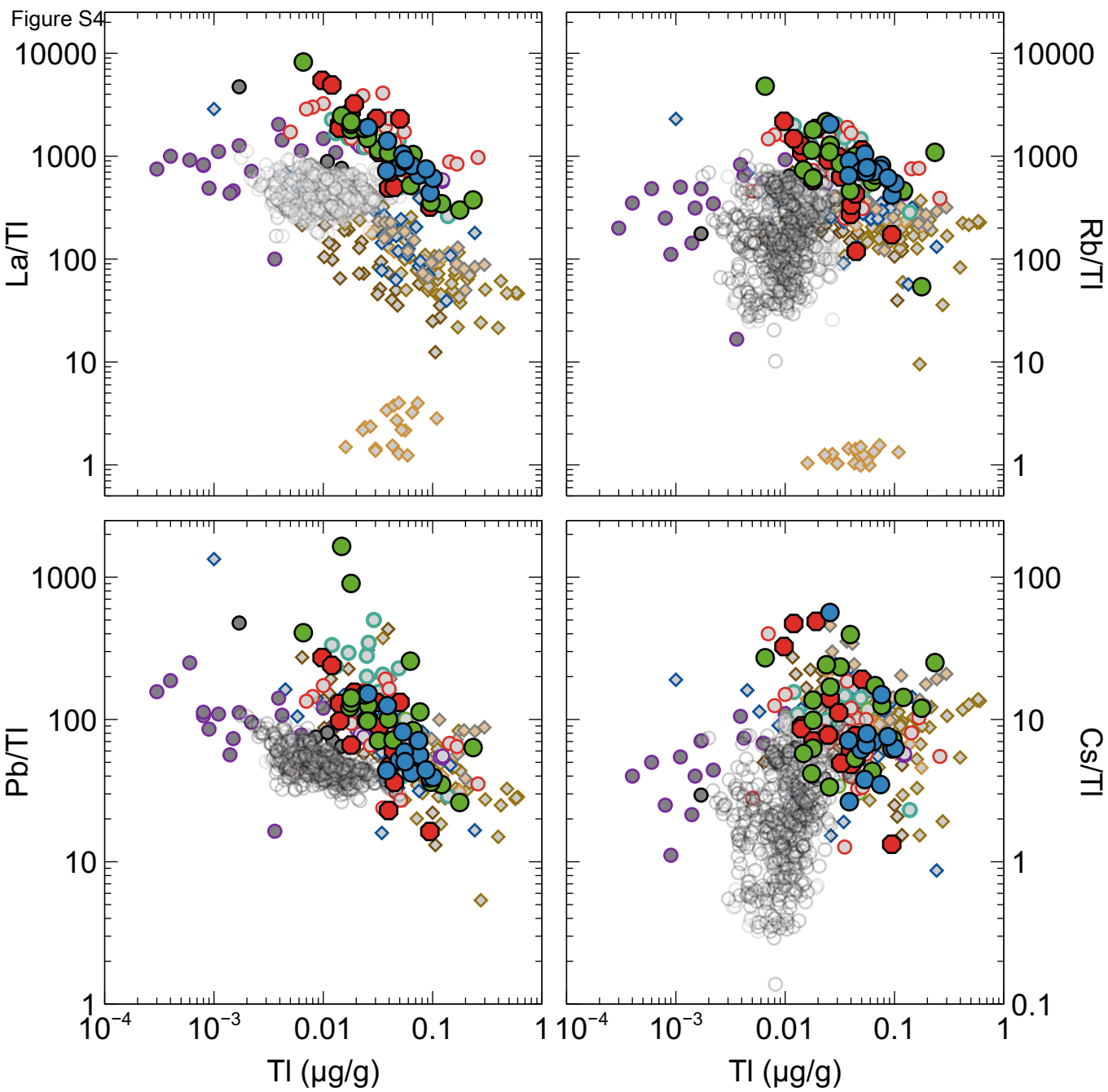


Figure 75

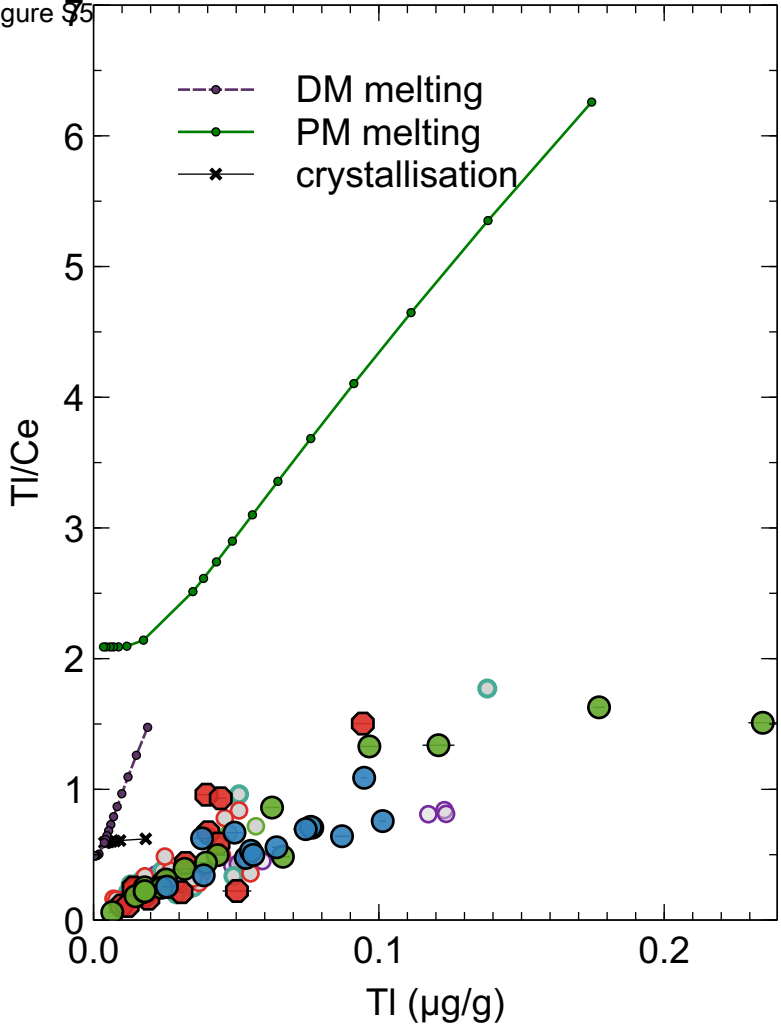


Figure 56

